THE ROLE OF NEUTRON ACTIVATION ANALYSIS IN THE PATHOLOGICAL EVALUATION OF SILVER-ELUTING BIOMEDICAL DEVICES IN BIOLOGICAL MATRICES

A Thesis

by

TREVOR WILCE LANCON

Submitted to the Office of Graduate and Professional Studies of
Texas A&M University
in partial fulfillment of the requirements for the degree of

MASTER OF SCIENCE

Chair of Committee,	Fred J. Clubb, Jr.
Co-Chair of Committee,	John W. Poston, Sr.
Committee Members,	John R. Ford, Jr.
	Bradley R. Weeks
Head of Department,	Yassin A. Hassan

August 2014

Major Subject: Health Physics

ABSTRACT

The purpose of this research was to determine the viability of using instrumental neutron activation analysis (INAA) to quantify silver nanoparticle (AgNP) content in biological matrices in the context of pathology evaluations of silver-eluting devices for United States Food and Drug Administration (FDA) approval. This work was comprised of feasibility, experimental, and simulation stages.

The extent of how AgNPs presented through transmission electron microscopy (TEM), scanning electron microscopy (SEM) with energy-dispersive X-ray microanalysis (EDX), and INAA methodologies within porcine skin was explored in the feasibility trial. Sections of skin containing control and test articles were investigated using these modalities. The control article was skin that contained a driveline coated in material known to elute AgNPs into tissue. TEM findings supported the conclusion that the host reacted to the presence of larger AgNP aggregates surrounding the control article at an ultrastructural level. The test article was skin that contained a driveline coated in material hypothesized to not elute AgNPs into surrounding tissue. AgNPs were not observed to aggregate throughout the tissue adjacent to the test article, and a marked host reaction to their presence was not observed. INAA results correlated with these findings; silver was not detected adjacent to the test article, but a concentration of 74 ppm ± 29% of silver was observed in tissue adjacent to the control article.

A complex system of ordinary differential equations (ODEs) was constructed to determine the inventory of the activation and subsequent decay progeny produced in a sample containing silver exposed to a neutron field. These ODEs were constructed into a Simulink® model and benchmarked using experimental data. This system was simplified after showing that production of induced ^{109}Ag during irradiation of silver did not significantly affect elemental silver estimation by measurement of ^{110m}Ag. Results from this model suggested that samples should be irradiated for up to 120 s and allowed to decay for 7 d before gamma ray spectroscopy is performed when investigating silver content in similar sodium-rich biological matrices via INAA in the future.

ACKNOWLEDGEMENTS

I would like to thank my committee chair, Dr. Clubb, my committee co-chair, Dr. Poston, and my committee members Dr. Weeks and Dr. Ford. They have all been very helpful throughout my college career and I can only hope to invest as much in my future colleagues as they have invested in me.

I greatly appreciate Karen Baker for her continual support and love, and I also thank my friends and co-workers for their contributions to the fond memories of my time at Texas A&M.

Finally, I cannot express how much I appreciate my parents for their enduring love and for all the opportunity they have provided for me.

NOMENCLATURE

AAS	Atomic Absorption Standard
AgNP	Silver Nanoparticle
CVP	Texas A&M Cardiovascular Pathology Laboratory
EDX	Energy-dispersive X-ray Microanalysis
FDA	Food and Drug Administration
HMDS	Hexamethyldisilazane
HPGe	High-Purity Germanium
INAA	Instrumental Neutron Activation Analysis
LM	Light Microscopy
LVAD	Left Ventricular Assist Device
NAA	Neutron Activation Analysis
NBF	Neutral Buffered Formalin
NSC	Texas A&M Nuclear Science Center
ODE	Ordinary Differential Equation
SDD	Silicon Drift Detector
SEM	Scanning Electron Microscopy
SNR	Signal to Noise Ratio
TEM	Transmission Electron Microscopy
THI	Texas Heart Institute
VAD	Ventricular Assist Device

TABLE OF CONTENTS

Page

LIST OF FIGURES

LIST OF TABLES

1. INTRODUCTION

1.1 Objective

The objective of this research is to determine the effectiveness of INAA as a means of quantifying silver concentration in biological matrices containing a silver nanoparticle-eluting biomedical device. This is of particular interest to applicable biomedical device manufacturers during preclinical trials for market approval. Thus, this research also aims to study how INAA correlates to other modalities more commonly used for pathology evaluations of implantable devices. Special consideration will be given to the context of manufacturers seeking the approval of the FDA. Another goal of this research is to develop a Matlab®/Simulink® program to model the dynamics of the progeny produced by neutron activation of natural silver.

1.2 Significance

A major problem encountered with implantable biomedical devices is the prevalence of bacterial infection following their implantation [1]. For example, ventricular assist devices (VADs) currently approved for human use require percutaneous drivelines to deliver power and control to the intracorporeal pumps via an external battery worn on the patient’s hip. Drivelines are particularly susceptible to bacterial and fungal infections and biofilm formation, and they provide an access point for undesirable organisms to enter hosts [2]. These infections pose a major threat to the efficacy of VADs and reduce positive patient outcome [3-5]. Estimates suggest that up to 50% of left ventricular assist device (LVAD) patients develop infections related to their device [6]. According to the second annual INTERMACS report, the most common cause of death in patients surviving at least one month on LVAD support is infection, resulting in 20.5% of deaths for over 1,000 patients [7]. In addition to decreasing treatment efficacy, high prevalence of driveline infection also increases the total financial burden of VAD therapy. Financial costs are estimated to double for patients that develop sepsis and increase more than sevenfold for patients that develop sepsis with pump housing infections and perioperative bleeding [8].

One way to combat infection is to coat or embed drivelines with various species of silver, which has well-documented antimicrobial properties [9, 10]. The exact mechanism of silver's antimicrobial activity is unknown, but it is widely accepted that silver ions generate DNA-damaging reactive oxygen species and disrupt membrane protein function and membrane permeability [11]. AgNPs, silver chloride, silver salts, and silver composites have all been studied as chemical media for the release of silver ions to biological targets [11]. One study comparing the ability of multiple forms of silver to inhibit bacterial growth suggests that silver chloride colloid is superior to both AgNPs and silver ions in isolated *Escherichia coli* cultures [12]. In more complex biological systems, however, AgNPs offer the ability to control the extent of migration and elution throughout tissue based mainly on the size distribution of the nanoparticles [10]. Thus, AgNPs are currently utilized as a means to reduce biofilm formation and bacterial migration along percutaneous drivelines, but it is important that the coating remains local to the line to avoid toxic effects potentially suffered by the patient.

Manufacturers must seek approval of the FDA prior to marketing biomedical devices in the United States. The FDA acts as a regulatory gauntlet, allowing biomedical devices to progress to market only after demonstrating a certain degree of efficacy and safety. The FDA also aims to aid manufacturers in developing products to promote the treatment of disease and ailments in the US. One way they accomplish this is by publishing guidance documents for industry that detail their expectations. The guidance document for industry innovators seeking approval of medical devices that include antimicrobial agents (including antimicrobial AgNPs) is scheduled for release in 2014. Among other parameters, this document recommends manufacturers characterize the toxicity of the antimicrobial agent used, the release kinetics of the agent, and its minimum effective concentration [13]. While routine pathology investigations such as light microscopy (LM) and TEM provide invaluable information related to these parameters, they lack the ability to quantify the amount of a given substance within a sample. INAA has been successfully correlated to LM and TEM data to quantify colloidal gold in mice [14]. This research aims to determine whether INAA will provide similarly useful information when correlated to TEM for studies involving silver in biological matrices. These data could be submitted to the FDA along with pathology data for manufacturers seeking market approval of their silver-coated devices.

1.3 Pathology Techniques

Many techniques are employed to investigate pathological changes to host tissues following biomedical device implantation. Pathologists at the Texas A&M Cardiovascular Pathology Laboratory (CVP) routinely interpret data from a variety of investigation modalities to determine how humans and animals respond to device applications at gross, cellular, and ultrastructural levels. The most commonly used techniques for this are gross examination, LM, TEM, and SEM/EDX. Gross examination is useful to determine whether significant changes are present at a local tissue site or within single- or multiple-organ systems. Microscopic examination is warranted when gross changes are present or simply as a tool to enhance diagnoses, whether they are positive or negative. Fig. 1 compares which techniques are most useful to see structures of various sizes. Gross examination is suitable when researchers desire to see structures with a submillimeter resolution. To resolve features on submicron and nanometer scales, light and electron microscopy are used, respectively.

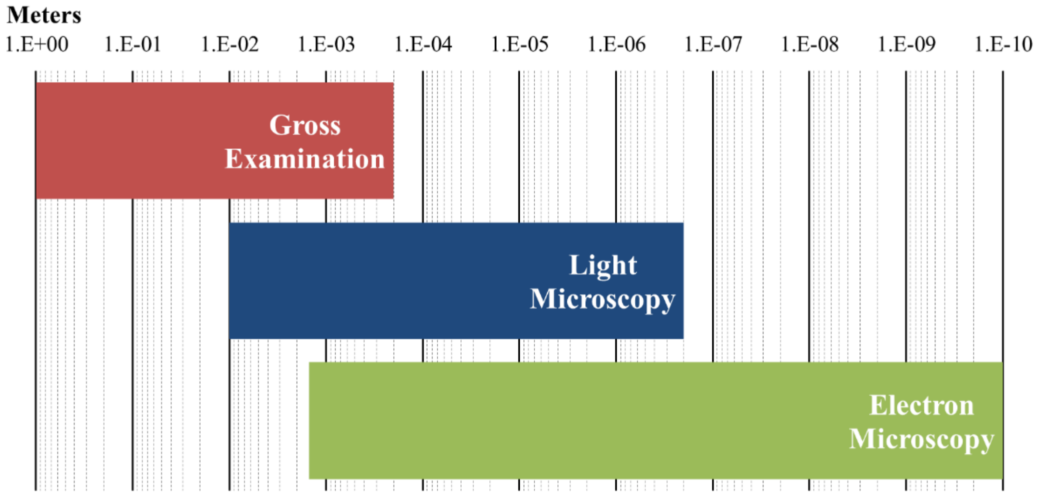

Fig. 1 Resolving power of different modalities used for pathological investigations

1.4 Electron Microscopy

Electron microscopy is performed when it is desirable to evaluate the ultrastructure of a specimen. TEM is utilized to view internal structures such as intracellular and extracellular components of biological specimens. Electrons are accelerated through an ultrathin section of tissue and detected as they emerge from the sample, generating an image in which grayscale depends on electron density of the area viewed. Preparing samples for TEM requires the samples be biologically fixed, dehydrated, infiltrated with a solvent, polymerized, and sectioned into 80 – 120 nm thick slices. These slices are stained with heavy metal solutions to increase the electron density of different structures, causing the electrons to attenuate more strongly in some areas of the tissue. Uranyl acetate and Reynolds' lead citrate are some commonly used metal stains in addition to osmium tetroxide, which also functions as a post-fixative for adipocytes and fatty tissue. The mechanisms behind the reactions of uranyl acetate and lead citrate with different tissues are poorly understood; however, these stains are noted to have an affinity for tissues post-fixed with osmium tetroxide prior to staining [15]. Lead citrate sometimes forms spherical precipitates within the tissues it stains that appear similar to AgNPs when viewed with TEM, as shown in Fig. 2 [16]. Thus, it is difficult to assess whether tissues contain AgNPs using TEM with no additional elemental discrimination since positive observations of highly attenuating spheres within biological samples may simply be caused by staining artifact. Some TEM systems are equipped with EDX systems, providing a means of reliable identification of elemental constituents within samples. Quantification of a measurand is also possible using this technique, but it requires detailed knowledge of sample geometry and a rigorous mathematical approach [17].

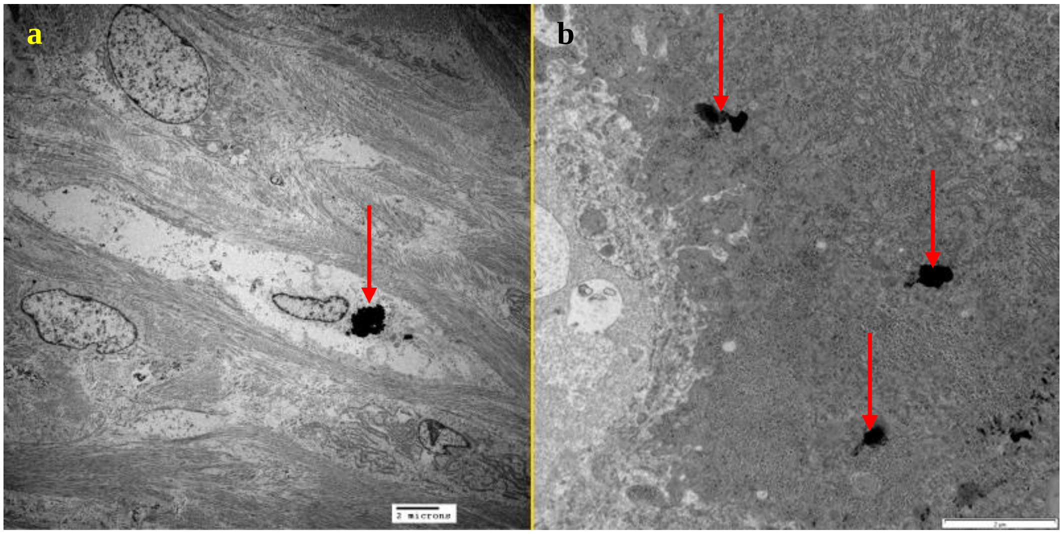

Fig. 2 Comparison of similarities between a AgNP aggregate and lead citrate precipitates in TEM. Red arrows point to an intracellular aggregate of silver nanoparticles in pig skin (a) and lead citrate staining artifact in rat liver (b). Scale bars are 2 μm

Quantifying nanoparticles with a TEM requires the distribution of nanoparticles and their aggregates to be spatially homogeneous on a scale comparable to the thickness of TEM sections. Fig. 3 illustrates some of the issues with analyzing TEM sections for nanoparticles when the size of the measurand is on the same scale as the section thickness. Section thickness is on the same order of nanoparticle size, making it difficult to accurately determine the amount of singular and aggregated nanoparticles within tissue based on TEM alone. For example, the uppermost aggregate (represented by an oval) intersects the sectioning line, and the entire cross-section of the aggregate is represented in Section A. Conversely, the true size of this aggregate would be underestimated if Section B were observed.

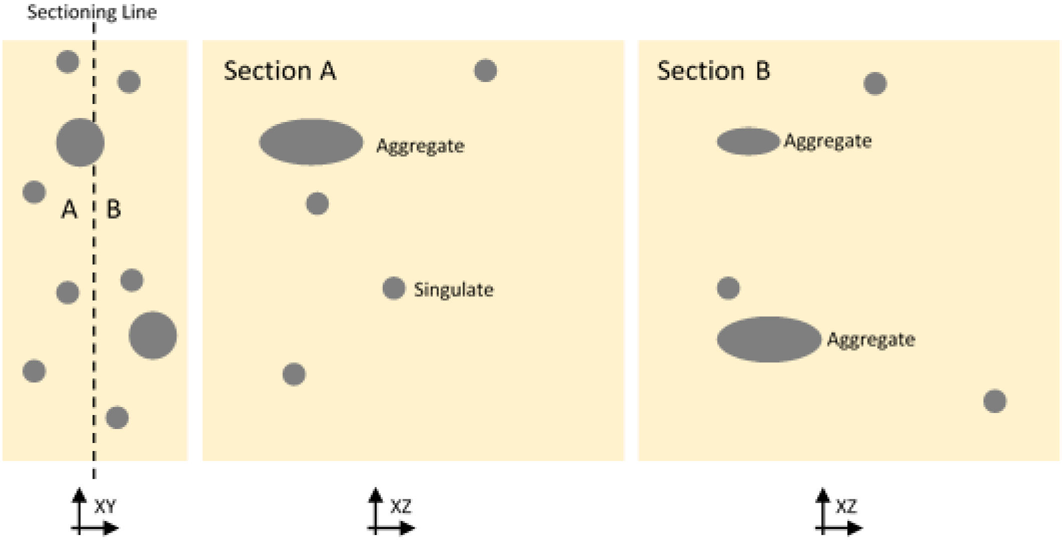

Fig. 3 Spatial heterogeneity of nanoparticle distribution between consecutive TEM sections

SEM is used to view surfaces of specimens that are either intact or that have been exposed by sectioning. Electrons are accelerated towards a bulk specimen and their backscatter or secondary electron distributions are used to generate an image of the surface. Backscatter detection is used to provide images in which grayscale is a function of elemental density (i.e., areas of low density appear to be dark compared to lighter areas representing high density). SEM preparation techniques are highly variable depending on the type of sample and laboratory capabilities. Techniques include biological fixation, dehydration, air or hexamethyldisilazane (HMDS) drying, desiccation, and mounting on carbon SEM stubs with double-sided tape. A low-vacuum chamber is sometimes used to scan surfaces of biological specimens to reduce sample charging and to avoid the need to coat the surfaces with conductive materials that could hinder elemental analysis and transferability to post-SEM histology. Elemental analysis is possible when SEM systems include EDX hardware, and the ability to discriminate between most elements when viewing sample surfaces is useful. Standardless quantification, however, is fraught with error and highly affected by sample surface geometry, as shown in Fig. 4 [18]. An ideal geometry is shown (diagram a Fig. 4), where P is the total X-ray path length from within the electron interaction volume to the EDX silicon drift detector and S is the length of the X-ray path that may be affected by attenuation. For samples with surface ridges (diagram b Fig. 4), the $S \cdot P^{-1}$ ratio may increase, causing an underestimation of a measurand that is present within the interaction volume. For samples with surface valleys (diagram c Fig. 4), the $S \cdot P^{-1}$ ratio may decrease and measurand concentration will be overestimated.

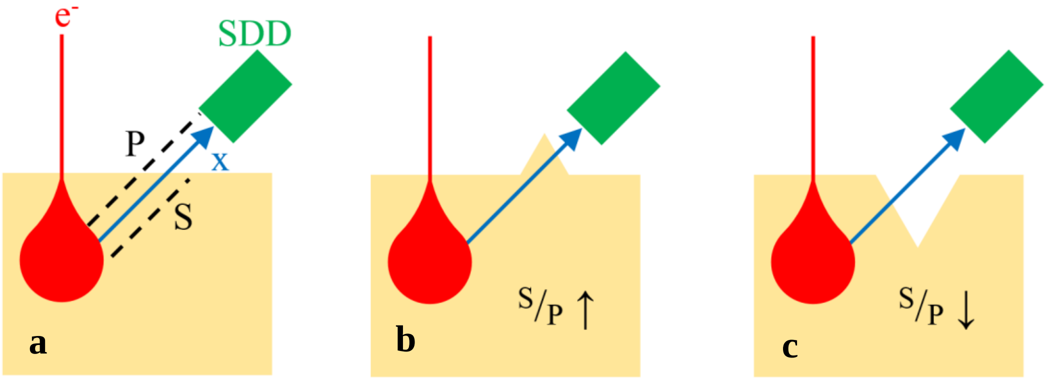

Fig. 4 Effects of sample surface geometry on EDX measurements for a flat surface (a), a ridge (b), and a valley (c)

Additionally, interaction volumes for electrons in silver vary significantly on the nanoscale. Adjusting electron beam potential in the SEM is necessary to achieve proper contrast at varying magnifications, but it may also greatly affect nanoparticle sampling volume and thus EDX results. Fig. 5 shows results from Monte Carlo simulations of electron interaction volumes in 100 nm diameter AgNPs performed using WinCasino (CASINO version 3, University de Sherbooke, Quebec, Canada). The 5 kV beam (image a Fig. 5) diverges significantly within the nanoparticle, and few electrons are shown escaping the bottom side of the nanoparticle. The 15 kV beam (image b Fig. 5) only slightly diverges as it travels through the nanoparticle, and most electrons are seen escaping its surface.

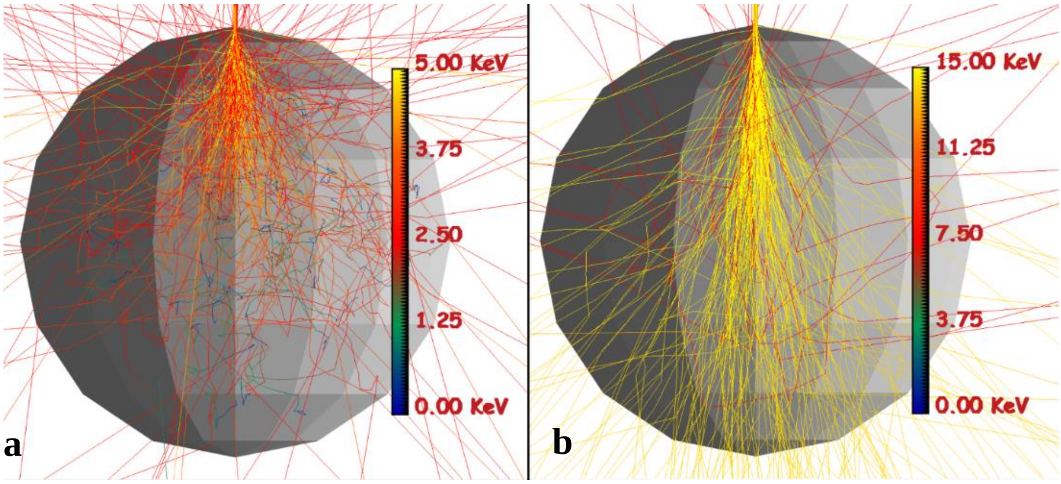

Fig. 5 Comparison of Monte Carlo simulations of 5 kV (a) and 15 kV (b) electron beams interacting in a 100 nm diameter silver nanoparticle

1.5 Neutron Activation Analysis

Neutron activation analysis (NAA) is an established method that can be used to quantify many elements to varying extents within bulk substrates or matrices [19]. Samples are subjected to a neutron field, and elements within the sample are activated and become radioactive. The resulting radionuclides that decay by emitting gamma rays of known energies can be detected with a gamma ray spectrometer and used to quantify the amount of a measurand within the sample. NAA performed without chemical separation of measurands from irradiated samples is commonly referred to as INAA. Quantification of an element can be performed by the absolute method. Eq. 1 is used to calculate the amount of a measurand solely based on the counts observed under a specific photopeak with otherwise known data [20]:

$$W_{SAM} = \frac{C_{SAM}^{i}}{\varepsilon^{i} I^{i}} \cdot \frac{\lambda M_a}{m_f N_a} \cdot \left[\left(1 - e^{-\lambda t_a}\right) \cdot e^{-\lambda t_d} \cdot \left(1 - e^{-\lambda t_c}\right) \cdot \phi \cdot \sigma\right]^{-1}, \tag{1}$$

where W_{SAM} is the mass of silver in the sample; C_{SAM} is the net counts under the i^{th} photopeak in the sample; ε is absolute detector efficiency for the i^{th} photopeak; I is the gamma ray intensity of the i^{th} photopeak; λ is the decay constant of the measurand; M_a is its atomic mass; m_f is its isotopic abundance ratio; N_a is Avogadro’s number; t_a is activation time; t_d is decay time; t_c is counting time; ϕ is neutron fluence rate; and σ is activation cross-section.

Neutron fluence rate and activation cross-sections are energy-dependent, but can be simplified into scalars or vectors representing effective values for a desired number of energy groups. Regardless, this method requires detailed knowledge of the neutron fluence rate distribution within a sample during activation and complete characterization of the inefficiencies of the spectrometer. Such information is not easily determined to a high degree of accuracy or is rarely available. If a standard with a similar matrix containing a known measurand concentration is irradiated under the same conditions as the sample of interest, the unknown mass of the measurand in the sample can be calculated using the comparator method:

$$W_{SAM} \pm U_{SAM} = W_{STD} \left(\frac{C_{SAM}}{C_{STD}} \left[1 \pm \sqrt{ \left(\frac{\sigma_{SAM}}{C_{SAM}} \right)^2 + \left(\frac{\sigma_{STD}}{C_{STD}} \right)^2 } \right] \right)^i, \tag{2}$$

where W_{STD} is the mass of silver in the standard; U_{SAM} is the propagated uncertainty of the calculated mass of silver in the sample; C_{STD} and σ_{STD} are the net counts and uncertainty of the i^{th} photopeak in the standard; and σ_{SAM} is the uncertainty of the i^{th} photopeak in the sample [20].

Experiments performed to measure silver in various matrices are summarized in Table 1. Reactors are often utilized for high neutron fluence rates, irradiation times range from 3 s to 6 h, and counting times range from 30 s to 20 h. The most commonly monitored reactions are:

$$\mathrm{n} + {}^{107}_{47}\mathrm{Ag} \rightarrow {}^{108}_{47}\mathrm{Ag} \xrightarrow{t_{0.5}=2.38\ \mathrm{m}} {}^{108}_{48}\mathrm{Cd} + \beta^- + \gamma, \tag{3}$$

$$\mathrm{n} + {}^{109}_{47}\mathrm{Ag} \rightarrow {}^{110}_{47}\mathrm{Ag} \xrightarrow{t_{0.5}=24.6\ \mathrm{s}} {}^{110}_{48}\mathrm{Cd} + \beta^- + \gamma, \tag{4}$$

$$\mathrm{n} + {}^{109}_{47}\mathrm{Ag} \rightarrow {}^{110\mathrm{m}}_{47}\mathrm{Ag} \xrightarrow{t_{0.5}=250\ \mathrm{d}} {}^{110}_{48}\mathrm{Cd} + \beta^- + \gamma. \tag{5}$$

Table 1 Summary of NAA experiment parameters found in the literature for biological and non-biological sample investigations

Author, Reference	Matrix Type	Thermal Neutron Fluence Rate [$\mathrm{n \cdot cm^{-2} \cdot s^{-1}}$]	Decay(s) Monitored	Irradiation Time [s]	Counting Time [s]
Adams [21]	Metallic	1.00E+12	^{110}Ag	< 30	< 900
Albini [22]	Particulate	3.50E+11	^{110}Ag	120	< 160
Sujari [23]	Biologic	1.00E+12	^{110m}Ag	21600	79200
Randa [24]	Biologic	8.00E+13	^{110m}Ag	< 18000	< 7200
Gordus [25]	Metallic	4.00E+04	^{108}Ag, ^{110}Ag	60	60
Swain [26]	Geologic	1.00E+13	^{110m}Ag	< 21600	n/a
Pun [27]	Geologic	2.30E+11	^{110}Ag	10	30
Pantelica [28]	Biologic	3.00E+13	^{110m}Ag	3600	< 72000
Fukushima [29]	Biologic	5.00E+11	^{110}Ag	15	60

The most commonly monitored gamma ray from activated biological samples containing silver is the 657 keV photopeak produced from the decay of ^{110m}Ag ($t_{0.5}$ = 250 d). An exception to this is shown in the experiment performed by Fukushima and Chatt [29]. These experimenters used Compton suppression during gamma spectroscopy to allow for rapid quantification of silver in oysters using the 657 keV photopeak produced by the much shorter-lived ^{110}Ag ($t_{0.5}$ = 24.6 s). Compton suppression is needed to perform rapid analysis with ^{110}Ag due to the high sodium content in biological matrices. The sodium activation reaction is a major Compton continuum contributor for gamma ray spectroscopy of activated biological samples:

$$\mathrm{n} + {}^{23}_{11}Na \rightarrow {}^{24}_{11}Na \xrightarrow{t_{0.5}=14.9\ \mathrm{h}} {}^{24}_{12}Mg + \beta^{-} + \gamma. \tag{6}$$

If Compton suppression is not a possibility, the ^{24}Na is usually allowed to decay significantly before counting is possible to a high degree of accuracy.

The monitored reaction and the irradiation, decay, and counting times are chosen based on how sensitive the element in question is to neutron activation and how its half-life compares to the half-lives of interfering radionuclides produced in the sample as byproducts. For this experiment, ^{110m}Ag is chosen as the silver isotope to monitor due to its long half-life compared to the ^{24}Na byproduct that is expected to be abundant in the sample after irradiation. Na-24 activity reduces to approximately 0.1% of its original value 150 h (ten ^{24}Na half-lives) after irradiation; however, ^{110m}Ag will only reduce to approximately 98% of its original activity in the same time. Additionally, in the context of a device manufacturer performing this analysis as a means to evaluate a product during a preclinical trial, it is desirable to keep service cost low and sample throughput high. Thus, irradiation time is kept to a minimum while post-irradiation and pre-counting decay times can be extended to allow for adequate ^{24}Na decay.

Natural silver consists of 51.84% ^{107}Ag and 48.16% ^{109}Ag, and both of these isotopes have significant neutron capture cross-sections as shown in Fig. 6. The cross-sections for ^{107}Ag and ^{109}Ag are similar for the majority of the resonance region; however, ^{109}Ag has a large resonance capture peak at 5.2 eV that ^{107}Ag does not. The thermal cross-section for ^{107}Ag is also lower than for ^{109}Ag. It should be noted that the cross-sections for ^{110m}Ag are comparable to those for ^{107}Ag and ^{109}Ag throughout the thermal and resonance energy ranges with exception of the 5.2 eV ^{109}Ag resonance.

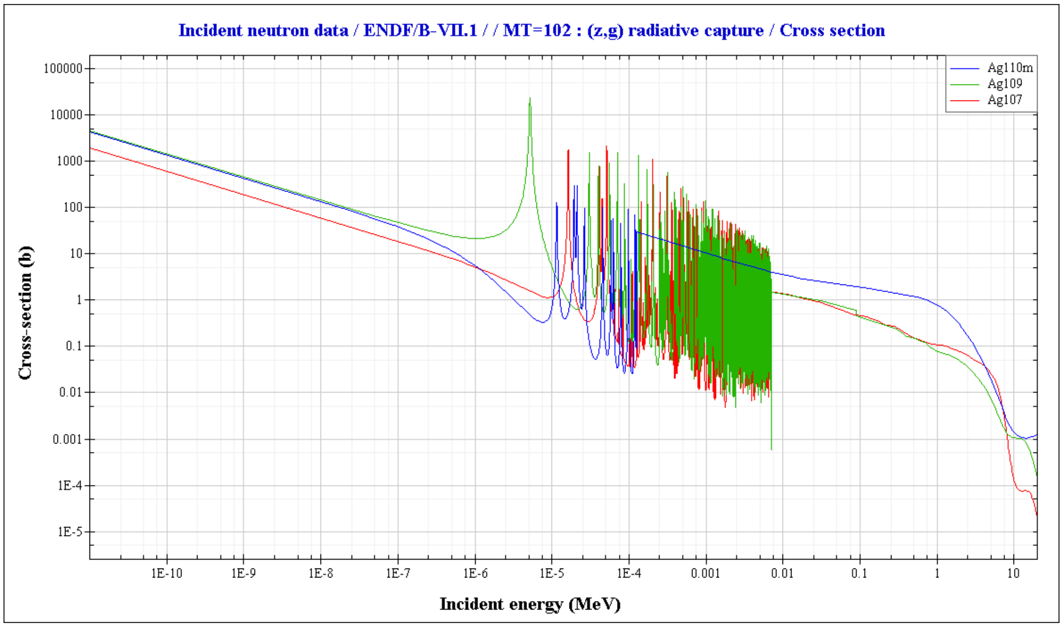

Fig. 6 Radiative capture neutron cross-sections for ^{107}Ag, ^{109}Ag, and ^{110m}Ag. Data was accessed from the ENDF/B-VII.2 database via Janis [30]

When a sample containing natural silver is introduced to a neutron field, ^{108}Ag and ^{110}Ag and their metastable states build up within the sample. These nuclides undergo radioactive decay to produce isotopes of cadmium and palladium, or they may double-capture to form ^{109}Ag and ^{111}Ag, respectively. Thus, the activation of silver produces a complex web of activation and decay products as shown in the diagram in Fig. 7.

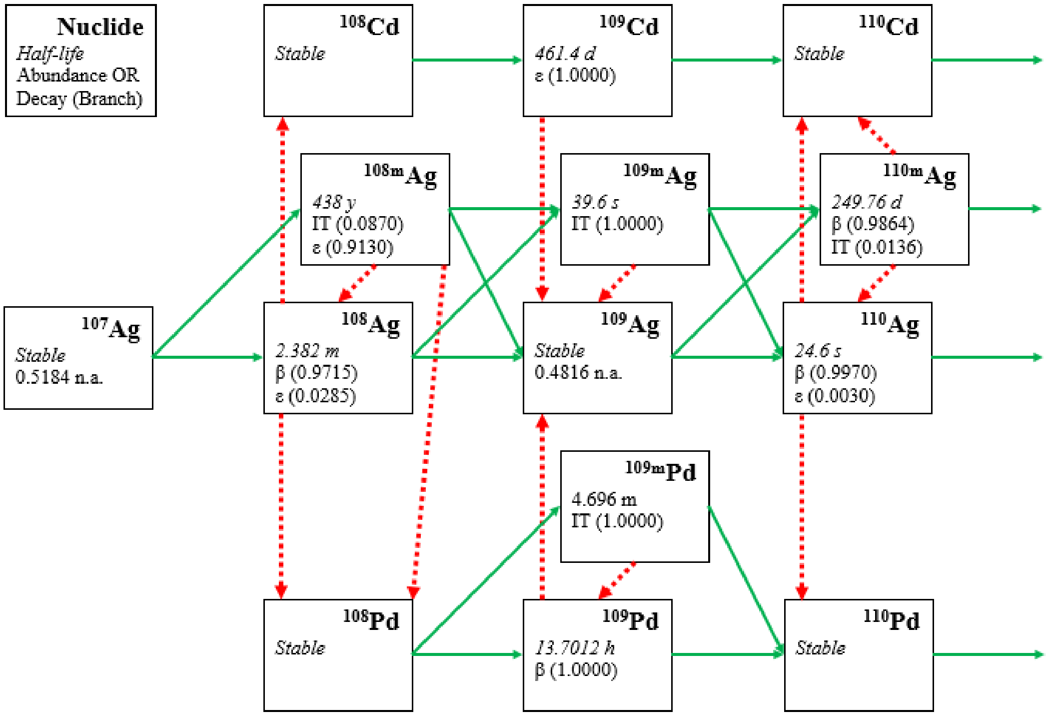

Fig. 7 Activation (solid green arrows) and decay (dotted red arrows) products resulting from the exposure of natural silver to a neutron field. Natural abundances are listed for ^{107}Ag and ^{109}Ag. Also listed are decay modes and half-lives for the radionuclides and their metastable states [31]. A legend is shown in the upper-left box labeled “Nuclide”

Pathways of most interest in Fig. 7 are those that contribute to the buildup of induced ^{109}Ag, such as those shown in Eqs. 7 – 9:

$$^{107}_{47}Ag \xrightarrow{activation} {}^{108}_{47}Ag \xrightarrow{activation} {}^{109}_{47}Ag, \tag{7}$$

$$^{107}_{47}Ag \xrightarrow{activation} {}^{108}_{47}Ag \xrightarrow{activation} {}^{109m}_{47}Ag \xrightarrow{IT\ decay} {}^{109}_{47}Ag, \tag{8}$$

$$^{107}_{47}Ag \xrightarrow{activation} {}^{108}_{47}Ag \xrightarrow{\beta^-\ decay} {}^{108}_{48}Cd \xrightarrow{activation} {}^{109}_{48}Cd \xrightarrow{EC\ decay} {}^{109}_{47}Ag. \tag{9}$$

Induced production of ^{109}Ag may cause false positive interference with the amount of ^{110m}Ag measured during gamma ray spectroscopy. If all ^{109}Ag is assumed to be natural and this induced production of ^{109}Ag is indeed significant, using the absolute method of INAA to measure silver may lead to overestimates of the concentrations reported after analysis. Another source of error may arise if ^{110m}Ag is produced from triple activation of ^{107}Ag as in the pathway described in Eq. 10:

$$^{107}_{47}Ag \xrightarrow{activation} {}^{108}_{47}Ag \xrightarrow{activation} {}^{109m}_{47}Ag \xrightarrow{activation} {}^{110m}_{47}Ag. \tag{10}$$

This may introduce false positive observation of silver if all measured ^{110m}Ag is assumed to be produced from ^{109}Ag. It should be noted that the interference processes described in Eqs. 7 – 10 are hypothesized to be more relevant for analyses performed with higher neutron fluence rates and longer irradiation times.

A system of coupled ODEs can be constructed from this diagram by considering each nuclide box to be a compartment that can either be “filled” or “emptied” by each activation or radioactive decay process that occurs. Solving this system results in the time-dependent inventory of each nuclide and their metastable states that may be produced when silver is neutron activated. This system is shown in Eqs. 11 – 24:

$$\left(\frac{dN}{dt}\right)^{Ag107} = m_0^{Ag} N_A \left(\frac{m_f}{M_A}\right)^{Ag107} - \phi(\sigma N)^{Ag107}, \tag{11}$$

$$\left(\frac{dN}{dt}\right)^{Ag108} = \phi\left(F_g \sigma N\right)^{Ag107} + (Y_{IT}\lambda N)^{Ag108m} - \phi(\sigma N)^{Ag108} - (\lambda N)^{Ag108}, \tag{12}$$

$$\left(\frac{dN}{dt}\right)^{Ag108m} = (F_m \sigma N)^{Ag107} - \phi(\sigma N)^{Ag108m} - (\lambda N)^{Ag108m}, \tag{13}$$

$$\begin{aligned}\left(\frac{dN}{dt}\right)^{Ag109} = {} & m_0^{Ag} N_A \left(\frac{m_f}{M_A}\right)^{Ag109} + \left(F_g \sigma N\right)^{Ag108} + \left(F_g \sigma N\right)^{Ag108m} + (\lambda N)^{Cd109} + \\ & (\lambda N)^{Pd109} + (\lambda N)^{Ag109m} - \phi(\sigma N)^{Ag109},\end{aligned} \tag{14}$$

$$\left(\frac{dN}{dt}\right)^{Ag109m} = (F_m \sigma N)^{Ag108} + (F_m \sigma N)^{Ag108m} - (\lambda N)^{Ag109m} - \phi(\sigma N)^{Ag109m}, \tag{15}$$

$$\begin{aligned}\left(\frac{dN}{dt}\right)^{Ag110} = {} & \left(F_g \sigma N\right)^{Ag109} + \left(F_g \sigma N\right)^{Ag109m} + (Y_{IT}\lambda N)^{Ag110m} - (\lambda N)^{Ag110} - \\ & \phi(\sigma N)^{Ag110},\end{aligned} \tag{16}$$

$$\left(\frac{dN}{dt}\right)^{Ag110m} = (F_m \sigma N)^{Ag109} + (F_m \sigma N)^{Ag109m} - (\lambda N)^{Ag110m} - \phi(\sigma N)^{Ag110m}, \tag{17}$$

$$\left(\frac{dN}{dt}\right)^{Cd108} = \left(Y_\beta \lambda N\right)^{Ag108} - \phi(\sigma N)^{Cd108}, \tag{18}$$

$$\left(\frac{dN}{dt}\right)^{Cd109} = \phi(\sigma N)^{Cd108} - \phi(\sigma N)^{Cd109} - (\lambda N)^{Cd109}, \tag{19}$$

$$\left(\frac{dN}{dt}\right)^{Cd110} = \phi(\sigma N)^{Cd109} + \left(Y_\beta \lambda N\right)^{Ag110} + \left(Y_\beta \lambda N\right)^{Ag110m} - \phi(\sigma N)^{Cd110}, \tag{20}$$

$$\left(\frac{dN}{dt}\right)^{Pd108} = (Y_\epsilon \lambda N)^{Ag108} + (Y_\epsilon \lambda N)^{Ag108m} - \phi(\sigma N)^{Pd108}, \tag{21}$$

$$\left(\frac{dN}{dt}\right)^{Pd109} = \left(F_g \lambda N\right)^{Pd108} + (\lambda N)^{Pd109m} - \phi(\sigma N)^{Pd109} - (\lambda N)^{Pd109}, \tag{22}$$

$$\left(\frac{dN}{dt}\right)^{Pd109m} = (F_m \lambda N)^{Pd108} - \varphi(\sigma N)^{Pd109m} - (\lambda N)^{Pd109m}, \tag{23}$$

$$\left(\frac{dN}{dt}\right)^{Pd110} = (\sigma N)^{Pd109} + (\sigma N)^{Pd109m} + (Y_\epsilon \lambda N)^{Ag110} - \phi(\sigma N)^{Pd110}, \tag{24}$$

where N is the number of atoms of a certain nuclide; m_0 is initial mass of an element; F_g is the fraction of activations resulting in a ground state; F_m is the fraction of activations resulting in a metastable state; and Y_ε, Y_β, and Y_{IT} are branching ratios for electron capture, beta decay, and internal transition processes; respectively. In the case that interference from these progeny and induced buildup of ^{109}Ag can be ignored, this system simplifies to the following:

$$\left(\frac{dN}{dt}\right)^{Ag109} = m_0^{Ag} N_A \left(\frac{m_f}{M_A}\right)^{Ag109} - \phi(\sigma N)^{Ag109}, \tag{25}$$

$$\left(\frac{dN}{dt}\right)^{Ag110m} = (F_m \sigma N)^{Ag109} - (\lambda N)^{Ag110m} - \varphi(\sigma N)^{Ag110m}, \tag{26}$$

which assumes that contribution to ^{110m}Ag inventory by induced ^{109}Ag is negligible and that only naturally-occurring ^{109}Ag contributes to the production of ^{110m}Ag. Loss of ^{110m}Ag to activation is still considered in the simple model due to its comparably large cross-section shown in Fig. 6.

Sodium activation kinetics are more straightforward and can be represented by:

$$\left(\frac{dN}{dt}\right)^{Na23} = \left(\frac{m_0}{M_A}\right)^{Na} N_A - \phi(\sigma N)^{Na23}, \tag{27}$$

$$\left(\frac{dN}{dt}\right)^{Na24} = \phi(\sigma N)^{Na23} - (\lambda N)^{Na24} - \phi(\sigma N)^{Na24}. \tag{28}$$

2. MATERIALS AND METHODS

This research was performed in three stages. First, a feasibility trial was performed with positive control samples to establish a qualitative standard for how silver nanoparticles appeared grossly and microscopically and study whether INAA could provide the necessary quantitative information. Second, an experimental trial was performed in which samples from two silver-coated driveline implant sites were studied for the amount of silver present using experience from the feasibility trial. Finally, a mathematical model was constructed to simulate the behavior of silver and its activation and decay products in a neutron field similar to that provided in the small sample irradiation port at the Texas A&M Nuclear Science Center (NSC).

2.1 Feasibility Trial

A sample of porcine skin was injected post-explant with a proprietary AgNP solution of unknown concentration and fixed in 10% neutral buffered formalin (NBF). NBF is an aqueous solution containing formaldehyde, methanol, and a sodium phosphate buffer (Cardinal Health Inc., Dublin, OH). Once fixed, the skin was delivered to CVP and gross photographs were taken of the sample before it was dissected into sections for TEM, INAA, and SEM/EDX as shown in Fig. 8. These samples were placed in Cassettes 1, 3, and 5, respectively, and submitted for processing for each modality. Fig. 8 also shows photographs of these sectioned samples.

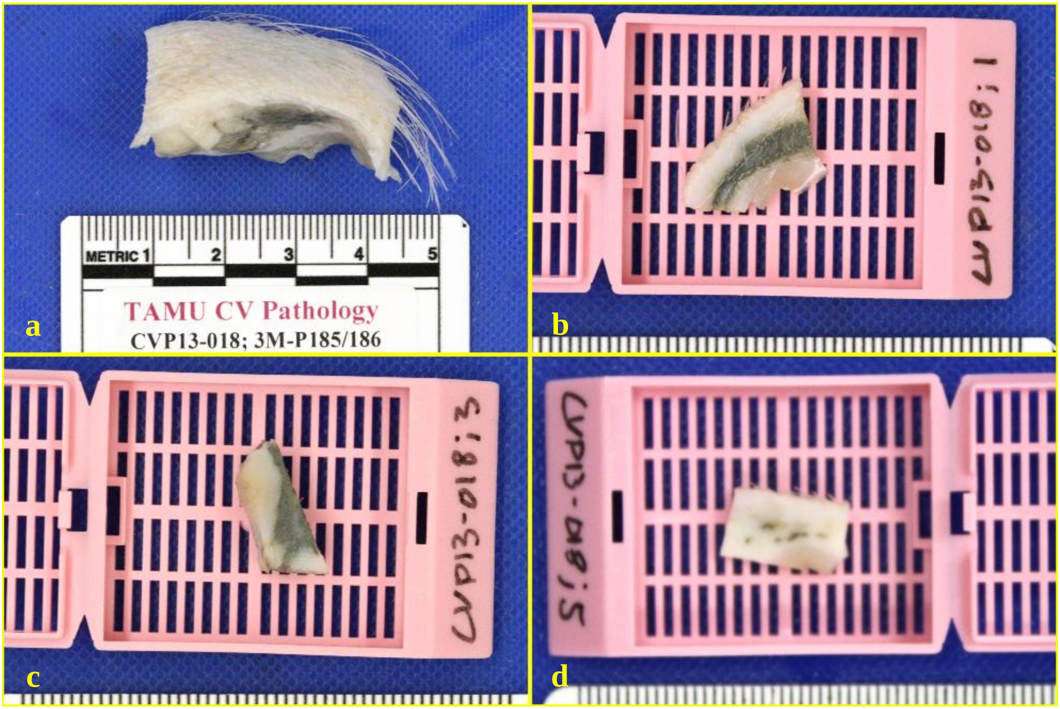

Fig. 8 Overview of the whole specimen and the samples taken for analysis. The whole specimen (a) was sectioned into pieces for TEM (b), INAA (c), and SEM/EDX (d). Ruler tick marks in photographs (b,c,d) are in millimeters

Cassette 1 was immersed in Trump's fixative and shipped to the Texas Heart Institute (THI) for TEM processing. Trump's fixative is an aqueous, sodium phosphate buffered solution containing a 4:1 ratio of formaldehyde to glutaraldehye [32]. The sample was post-fixed in osmium tetroxide and dehydrated in a series of aqueous solutions with increasing ethanol concentrations. It was embedded in a Poly/Bed 812 (Polysciences, Inc., Warrington, PA) plastic resin block before 80 nm sections were cut and mounted on 100 mesh copper grids. These sections were stained with uranyl acetate and lead citrate. Images were taken with a JEM 1250 (JEOL USA, Inc., Peabody, MA) electron microscope and delivered to CVP for observation of ultrastructural characteristics of the samples by a pathologist.

Cassette 3 was delivered to the NSC in formalin for INAA preparation. The sample was removed from formalin, weighed, and double-sealed within two polyethylene vials. Similarly, two double-sealed polyethylene vial samples were filled with 1 µL each silver nitrate-based atomic absorption standard (AAS) containing 987 ppm silver (Sigma Aldrich Corp., St. Louis, MO). All three vials were successively irradiated for 60 s in the D2 sample irradiation port of the NSC TRIGA Mark I reactor while it operated at 1 MW power. Samples were allowed to decay for 1 d before acquiring gamma ray spectra for 600 s of live time each in a high-purity germanium (HPGe) detector equipped with a multi-channel analyzer and a computer with GENIE™ 2000 software (detector and software from Canberra Industries Inc., Meriden, CT). Gamma ray spectra were analyzed in GENIE™ by 2nd differential peak location and non-linear least-squares fitting peak area calculation algorithms. Gamma ray peak identification was automated in GENIE™ using the standard nuclide identification library and unidentified peaks were further analyzed manually. The detector was previously calibrated for energy and efficiency with ^{152}Eu and ^{60}Co sources, respectively, by NSC personnel. When the 657 or 884 keV peaks were observed, the amount of silver in the tissue sample was calculated using Eq. 2.

The tissue from Cassette 5 was submitted for SEM/EDX and dehydrated in a series of aqueous solutions with increasing ethanol concentrations. The sample was allowed to dry in air until surfaces no longer glistened, then subjected to vacuum desiccation for further drying. Once dry, the sample was mounted on a carbon stub with double-sided conductive carbon tape and analyzed in a TM-3000 Tabletop SEM (Hitachi High Technologies America, Inc., Dallas, TX) equipped with an XFlash® silicon drift detector (SDD) and Quantax® EDX analysis software (detector and software from Bruker Biosciences Corp., Billerica, MA). SEM images and EDX spectra were acquired with 5 and 15 keV electron beams on both low- and high-current modes as deemed fit for each sample. EDX detector live time ranged from 128 – 158 s for all spectra acquired. X-ray peak identification and elemental mapping was automated in Quantax®; in addition, unidentified peaks were analyzed manually. The SDD was previously calibrated for energy using a copper calibration control.

2.2 Experimental Trial

Two driveline segments were explanted from a porcine model 43 d post-implant at a remote facility as part of a preclinical study conducted by an industry investigator. Each driveline was wrapped in velour that served as the interface between the device and the host's skin. One driveline's velour was coated in a AgNP solution that was known to leech into surrounding tissue (control article; Site 5). The other driveline was coated in a AgNP solution that was hypothesized to stay local to the device and not leech into surrounding tissue (test article; Site 3). Upon explant, each site consisted of a driveline embedded in approximately 55 cm^3 of porcine skin, or plugs. These plugs were fixed in 10% NBF before delivery to CVP. Gross photographs and radiographs were taken of the plugs before they were dissected into sections for TEM, INAA, and SEM/EDX as shown in Fig. 9. These samples were placed in labelled cassettes and submitted for processing for each analysis modality. Cassettes taken from Site 3 and Site 5 are shown in Appendix A. Sectioned strips of tissue are labeled with numbers (black) in the locations from which corresponding cassettes were collected. Cassettes are labeled (yellow) with the modality for which each was prepared. Unlabeled cassettes were not processed.

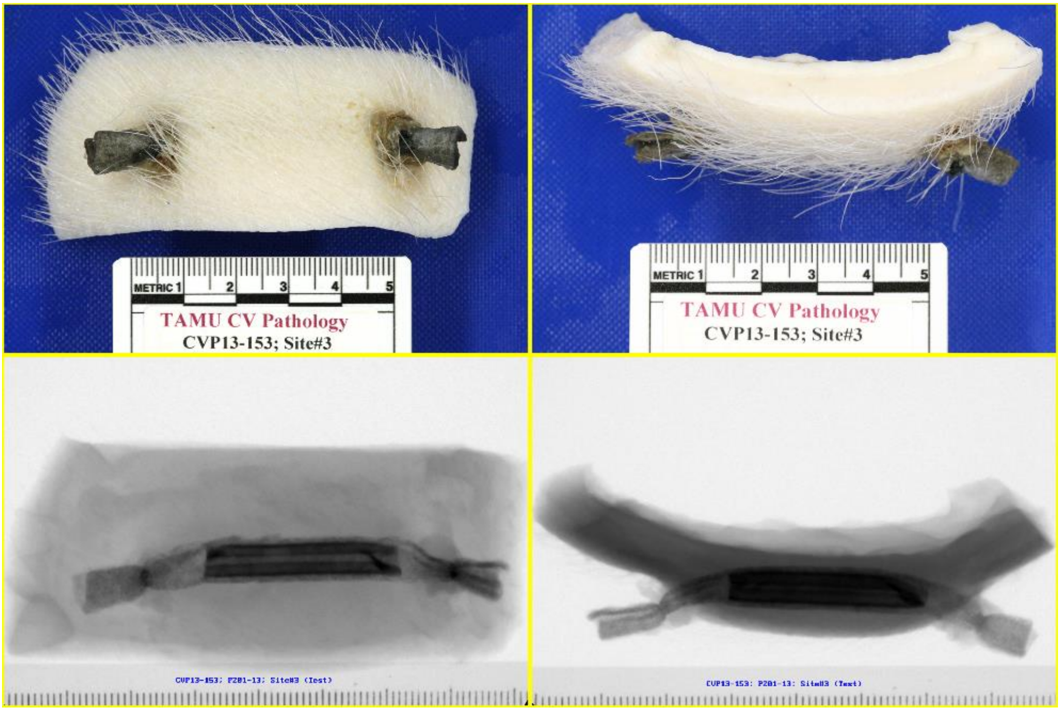

Fig. 9 Comparison of gross and radiographic appearances of the test article

Cassettes 2 and 11 were immersed in Trump's fixative and shipped to THI for TEM processing. The same protocol was used to process and analyze these samples as was used in the feasibility trial.

Cassettes 3, 6, 9, 12, 15, 18 were immersed in Trump's for further fixation. Prior to INAA processing, the fixative within the samples was replaced with 70% aqueous ethanol in an attempt to decrease the amount of sodium present within the samples during irradiation. Achieving a decrease in sodium content at the time of gamma ray acquisition was desired to reduce the background behind the measurand peaks and reduce gamma radiation exposure to NSC staff during sample handling. Samples were delivered to the NSC, removed from 70% ethanol, weighed, and double-sealed in polyethylene vials along with two 1 µL samples of the 987 ppm silver nitrate AAS. All vials were successively irradiated for 40 s each in the D2 sample irradiation port of the NCS TRIGA Mark I reactor with the reactor operating at 1 MW power. Samples were allowed to decay for approximately 6 d before acquiring gamma ray spectra for 600 s of live time each in a HPGe detector equipped with a multi-channel analyzer and a computer with GENIE™ 2000 software. The detector was previously calibrated for energy and efficiency by NSC personnel with ^{152}Eu and ^{60}Co sources, respectively. Other than the aforementioned changes in the fixation protocol and irradiation and decay times, the remainder of the analysis performed was the same as the feasibility trial.

Cassettes 1, 4, 7, 10, 13, 16 were submitted for SEM/EDX and dehydrated in a series of aqueous solutions with increasing ethanol concentrations. An absolute ethanol wash was followed with HMDS drying before the samples were allowed to air dry in an attempt to reduce drying artifact. After HMDS and air drying, all samples were desiccated in vacuum. Cassettes 1, 4, and 7 were mounted on a single large SEM stub with double-sided carbon tape; Cassettes 10, 13, and 16 were prepared similarly. The TM-3000 SEM was used to analyze all samples the same way the samples were analyzed in the feasibility trial with EDX acquisition live times ranging between

11 – 520 s for all spectra obtained. X-ray peak identification and elemental mapping was automated in Quantax®; in addition, unidentified peaks were analyzed manually. The SDD was previously calibrated for energy using a copper calibration control.

2.3 Simulation

A compartmental model was constructed in Matlab®/Simulink® (Version R2011a, MathWorks, Inc., Natick, MA) to calculate the inventory of each concerned radionuclide produced during neutron activation of silver and sodium and the progeny produced by subsequent radioactive decay. The model contained modules to initialize sample and activation parameters including neutron fluence rate, amount of elemental silver and sodium prior to irradiation, irradiation time, decay time, and counting time. These input modules are shown in Fig. 10 and Fig. 11. In Fig. 10, the "Switch" block changed the fluence rate to zero when the time on the simulation clock reached a value specified by the user, ending irradiation. The "Goto" block allowed wireless communication between this module and the rest of the model. Initial silver amount was specified in milligrams and converted to atoms, then communicated to the ODE modules with the "Goto7" block. In Fig. 11, the "Integrator5" block accumulated decays undergone by ^{110m}Ag once the time specified by the user in the "Switch1" block reached a certain value. The "Ag10m detected" functions multiplied these decays by branching ratios and detector efficiencies associated with the 657 and 884 keV peaks from ^{110m}Ag. The "…Counts" scopes displayed the total number of counts registered by the simulated detector for each energy channel.

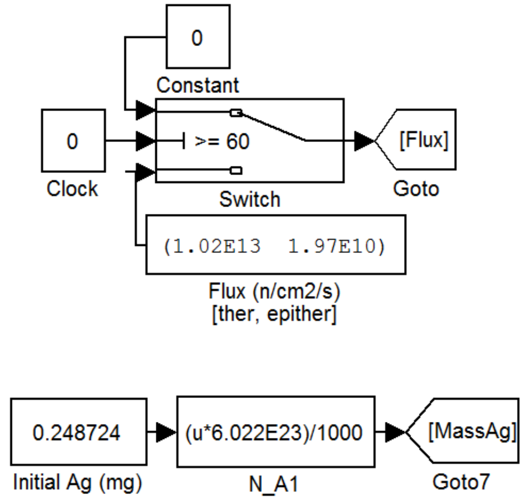

Fig. 10 The fluence rate controller and elemental silver initiation modules

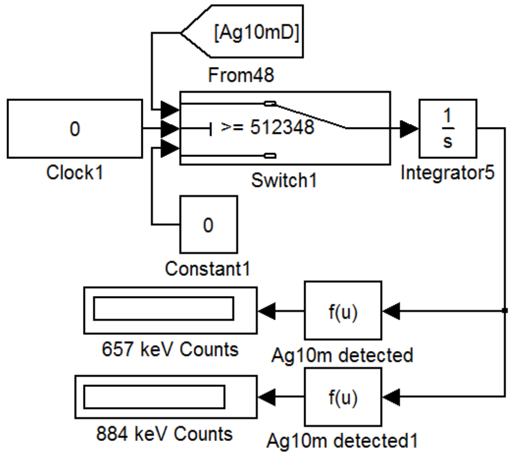

Fig. 11 The detector simulator

The model also contained modules for each compartment, or isotope, that accepted “wireless” inputs and output the inventory at each time step calculated. Examples of this are shown in Fig. 12 and Fig. 13. In Fig. 12, the “From34”, “From30”, and “From29” blocks transferred contributions to ^{110}Ag inventory from other activation and decay processes accounted for elsewhere in the model after branching ratios and metastable yields were calculated. The "Ag10A (cm2)" block accounted for loss from neutron activation when multiplied by the fluence rate value communicated via "From28" block, and "Ag10D (/s)" accounted for radioactive decay. "Add9" accumulated changes to the inventory from all processes during each iteration. Inventory was displayed in atoms as well as with a scope. A scope output is shown in Fig. 13. To generate this plot, the complex simulation was performed with an activation time of 60 s and total time of 300 s, then the "Ag10 (atoms)" block from Fig. 12 was viewed. ^{110}Ag inventory peaked at 60 s, and 240 s after irradiation (approximately ten ^{110}Ag half-lives) the inventory was nearly depleted.

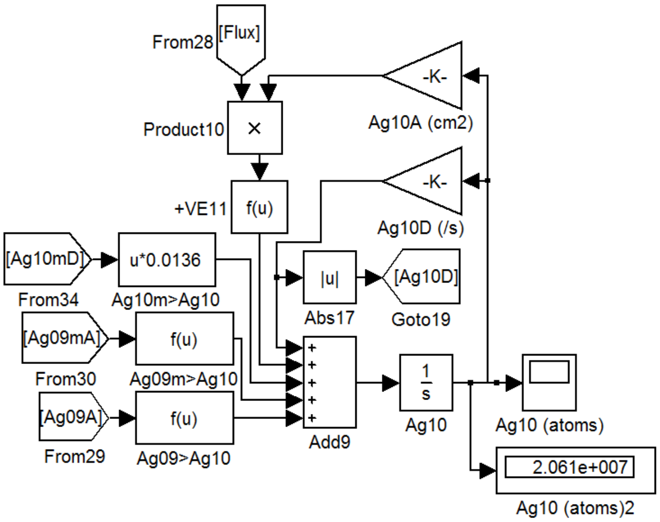

Fig. 12 The module used to calculate ^{110}Ag activity

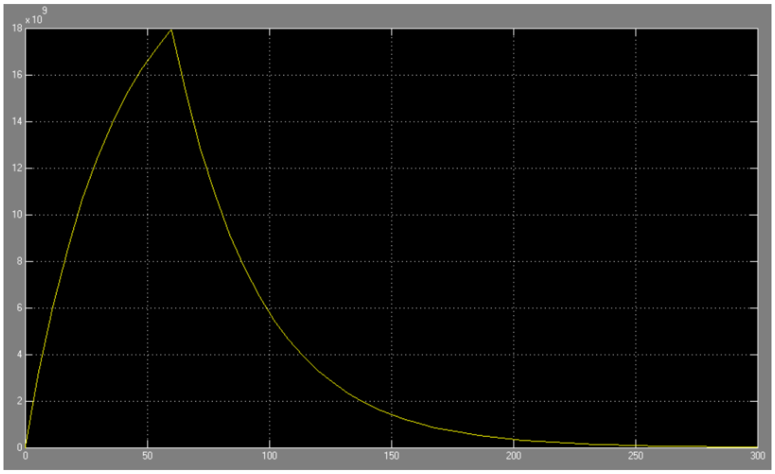

Fig. 13 Example of Simulink® scope output. Time is shown in seconds on the abscissa and ^{110}Ag inventory is in atoms on the ordinate

The complex model is shown in its entirety in Appendix B, and the simple model is shown in Appendix C. The complex version of the model was used to solve the coupled ODEs in Eqs. 11 – 24 with the ODE45 4th order Runge-Kutta solver native to Matlab®. Automatically optimized variable time steps and a relative error tolerance of 10^{-3} were used. A simplified version of the model was used to solve Eqs. 25 and 26 using the same parameters. Both models were used to solve Eqs. 27 and 28 to simulate sodium activation. Results from the feasibility and experimental trials were used to benchmark the computational models and determine which fluence rate scheme produced the best results. Results from the complex and simple systems were compared to determine the extent of error introduced by the assumptions made for the simple model.

Radiative neutron capture cross-sections and metastable isomer yield ratios were obtained from the TENDL-2013 library via Janis [33]. An exception was the data for the

^{109}Ag(n,γ)^{110m}Ag reaction, which was experimentally determined by Nakamura, et. al. [34]. Only thermal ($10^{-5} < E < 0.5$ eV) and resonance ($0.5 < E < 10^{5}$ eV) cross-sections were found to be significant, and fast activation processes were neglected. Thus, a two-group fluence rate scheme was utilized as a compromise between computational ease and accuracy.

Tested fluence rate values were based on the measurement and simulation results reported by Parham [35]. Parham measured thermal and epithermal fluence rates of 7.50×10^{12} and 2.40×10^{11} $\mathrm{n\cdot cm^{-2}\cdot s^{-1}}$, respectively, in the small sample irradiation port D2 at the NSC reactor. MCNP simulations determined thermal and epithermal fluence rates to be 1.02×10^{13} and 2.37×10^{11} $\mathrm{n\cdot cm^{-2}\cdot s^{-1}}$, respectively. Since cross-section values were obtained as resonance integrals, epithermal fluence rate was converted to resonance fluence rate for one of the tested schemes using Eq. 29 and the assumption that the resonance fluence rate distribution in the NSC core follows the E^{-1} assumption for light water reactors [36].

$$\phi_{epi} = \int_{E_{lower}}^{E_{upper}} \varphi(E)\, dE = \phi_{RI} \ln\frac{10^5}{0.5} = 12.2\phi_{RI} \rightarrow \phi_{RI} = \frac{\phi_{epi}}{12.2}, \tag{29}$$

where ϕ_{epi} is epithermal fluence rate; ϕ_{res} is the resonance fluence rate; $\varphi(E)$ is the fluence rate distribution; and E_{lower} and E_{upper} are the energy bounds of the resonance region. The simulation was solved with various fluence rate schemes until the most agreeable results were obtained.

The degree of difference between experimental and simulated results was determined by calculating ratios of the difference of experimentally determined net peak area to simulated net peak area as shown in Eq. 30:

$$R^i = \left(\frac{|A_{sim} - A_{exp}|}{A_{exp}}\right)^i, \tag{30}$$

where R^i is the degree of difference for the i^{th} photopeak and A_{exp} and A_{sim} are the net peak areas for experimental and simulated results of the i^{th} photopeak, respectively. Net peak areas for the ^{110m}Ag photopeaks at 657 and 884 keV were both used for this determination. This metric was used as a benchmark for the compartmental model.

Eq. 31 was used to compare results predicted by the simple and complex models:

$$\mathcal{R} = \left(\frac{|N_{spl} - N_{cpx}|}{N_{cpx}}\right)^{Ag-110m}, \tag{31}$$

where $\mathcal{R}$ is the degree of difference between the models and N_{spl} and N_{cpx} are the simulated ^{110m}Ag inventories at 7 d following the beginning of irradiation for the simple and complex models, respectively. The simulation was run for 7 d of total time, and irradiation time was varied from 10 to 1000 s. The degree of difference between the complex and simple models was calculated using Eq. 31 and plotted as a function of the fraction of total analysis time spent in irradiation. The model was used to support suggestions for modifications to potential future experiments by simulating and comparing ^{110m}Ag inventories for various suggested timing schemes.

3. RESULTS AND DISCUSSION

Results from the three stages of research are presented here. Images and INAA analysis results are reported for the feasibility and experimental trials. The computational model benchmarking and analysis results are presented as well.

3.1 Feasibility Trial

Representative transmission electron micrographs of the AgNP-injected pig skin taken in Cassette 1 are shown in Fig. 14. Intracellular (micrographs a, b Fig. 14) and extracellular (micrograph c Fig. 14) AgNPs were visible. High magnification (micrograph d Fig. 14) also showed individual AgNPs within an aggregate. Tissue reaction to AgNPs was not observed due to the injection occurring post-mortem; all observed AgNP behavior and localization was strictly due to diffusion and chemical processes. Suspected AgNPs ranged from small and singular to large and clustered. These images suggested that AgNPs were difficult to distinguish from surrounding metal-stained morphology at low magnifications unless they were clustered together to form larger, dense aggregates. Aggregation affinity also appeared to be nonspecific to location within or outside of cellular compartments. These images simply served as a control to familiarize the experimenters with AgNP appearance. In addition, they enabled a better understanding of how ultrastructural localization of AgNPs may be affected by pathological processes in the experimental trial.

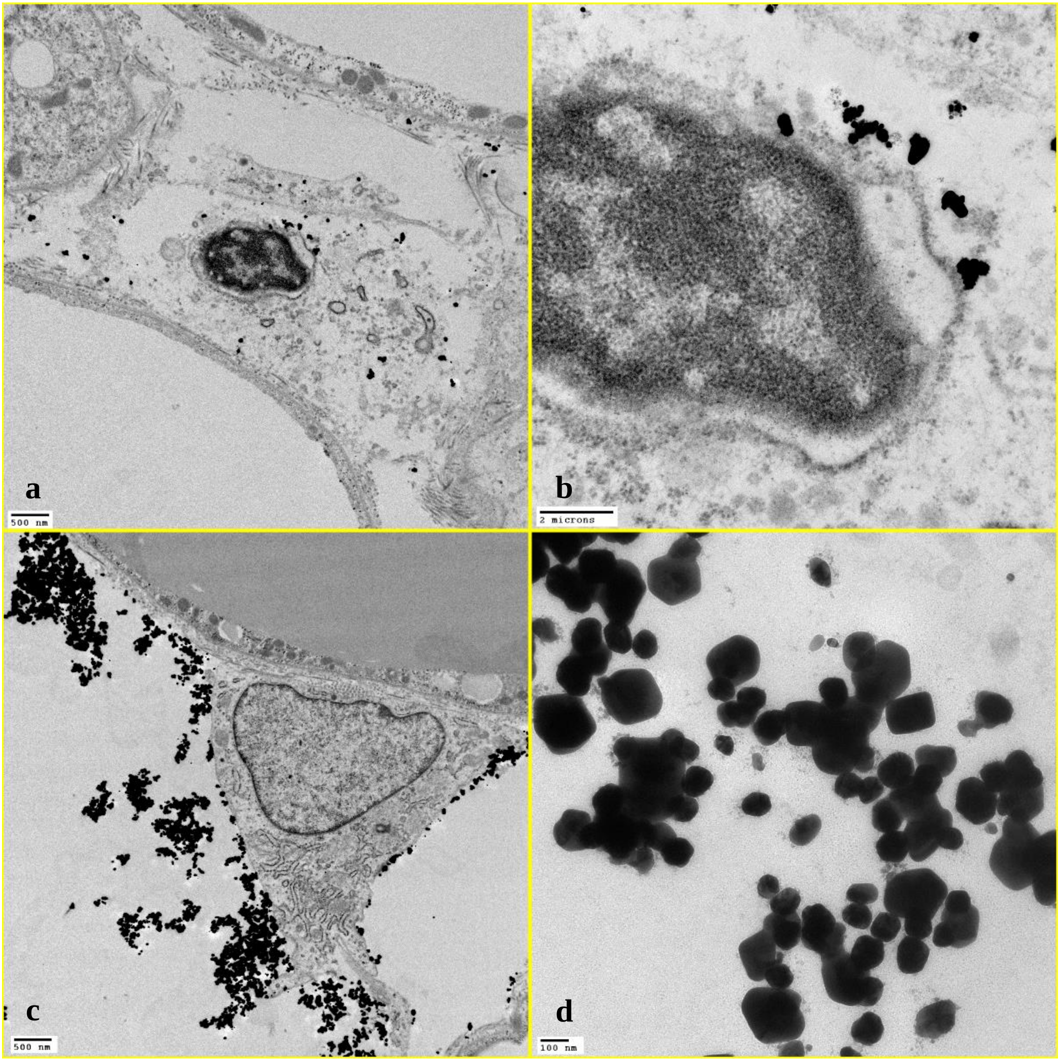

Fig. 14 The appearance of AgNP in TEM images is standardized in this figure. Scale bars are 500 nm (a,c), 2 µm (b), and 100 nm (d)

Cassette 3 was subjected to NAA; results from automated spectrum analysis in GENIE™ are shown in Table 2. The mass of silver in each standard was calculated using the 987 ppm silver concentration reported in the documentation of the standards. The amount of silver in the sample in Cassette 3 was calculated using both 657 and

884 keV peak data with each standard and Eq. 2. Results of these calculations are shown in Table 3.

Table 2 Peak analysis results from GENIE™ for the two standards and section of tissue subjected to INAA during the feasibility trial

Sample Descriptor	**Total Sample Mass [g]**	**Silver Mass [μg]**	**657 keV Peak Area [counts]**	**884 keV Peak Area [counts]**
Standard A	0.2052	202.5	758 ± 30.50	511 ± 23.57
Standard B	0.1990	196.4	756 ± 30.33	476 ± 24.13
Cassette 3	0.2996	N/A	7890 ± 147.84	4760 ± 140.05

Table 3 The amount of silver present in the feasibility skin sample

	Standard A	**Standard B**
657 keV Peak	2108 ± 93.57 μg	2050 ± 90.77 μg
884 keV Peak	1887 ± 103.22 μg	1964 ± 115.12 μg

A noticeable feature of the values reported in Table 3 is that using the 884 keV peak to quantify silver resulted in lower amounts than using the 657 keV peak. Furthermore, the error associated with the 884 keV peak calculations was higher for both standards. Fig 15 shows a comparison of the gamma ray spectra obtained from counting Standard A (spectrum a Fig 15) and Cassette 3 (spectrum b Fig 15). In contrast to the spectrum from Standard A, The spectrum from the sample in Cassette 3 displayed a background dominated by the 1386 and 2754 keV peaks emitted by ^{24}Na from within the sample. The Compton continuum from these peaks had a significant presence that was thought to mask the 657 and 884 keV ^{110m}Ag peaks used in this analysis. Since the 884 keV peak had a lower intensity, its signal did not stand out as well from the background caused by ^{24}Na. A signal-to-noise ratio (SNR) was computed using the

GENIE™ output of net area and continuum counts for each peak; these values are shown in Table 4. Correlating results shown in Fig 15 and Table 4, it was concluded that ^{24}Na was the major source of background causing poor SNR and therefore, the strong presence of ^{24}Na in the skin samples significantly contributed to silver measurement error.

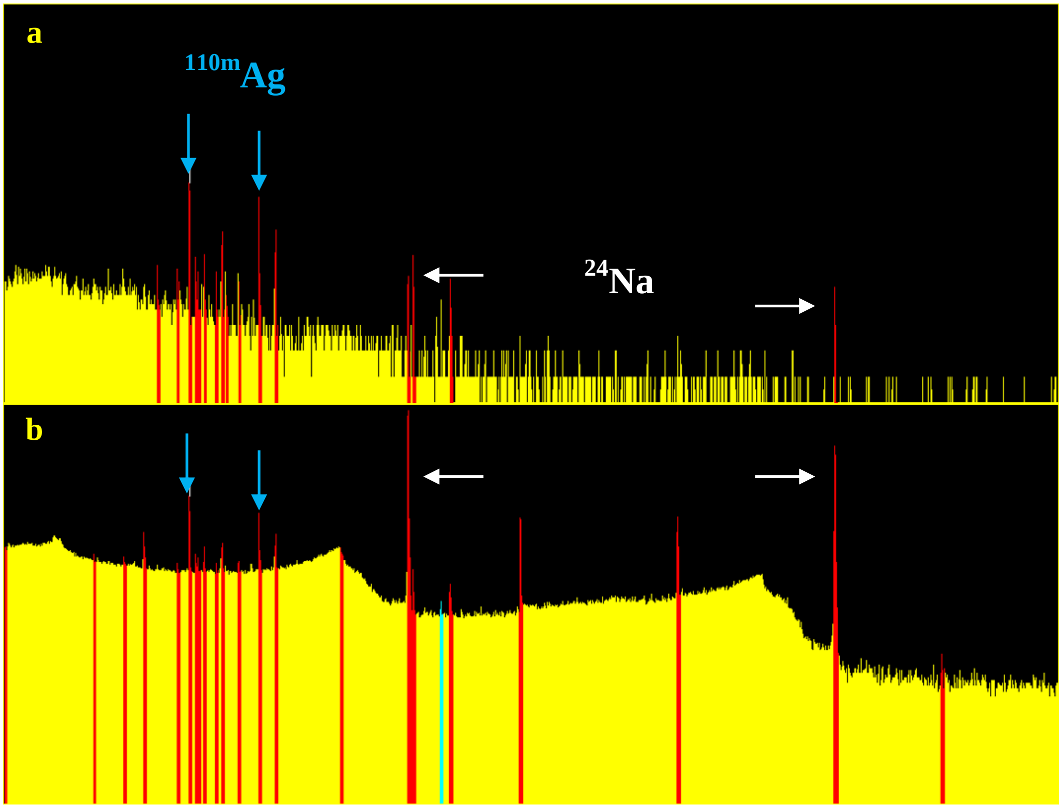

Fig 15. Feasibility trial gamma ray spectroscopy output provided by GENIE™. The gamma ray spectrum from Standard A (a) is compared to the spectrum acquired from Cassette 3 (b). Abscissae are energy and ordinates are net counts. The ^{110m}Ag and ^{24}Na peaks used in the analysis are noted by blue and white arrows, respectively

Table 4 The SNR for each measured silver peak and each sample from the feasibility trial

	Standard A	**Standard B**	**Cassette 3**
657 keV Peak	13.7	12.9	1.8
884 keV Peak	37.6	14.0	1.0

SEM with EDX was performed on the sample in Cassette 5; representative images from this analysis are shown in Fig. 16. A localized region of high contrast was noted from a low magnification (micrograph a Fig. 16) and was determined to be silver using EDX (elemental overlay b Fig. 16). High magnification of the surface showed randomly dispersed areas of high contrast varying in size (micrograph c Fig. 16) which were also shown to be silver using EDX (elemental overlay d Fig. 16). In this case, SEM itself did not provide detail that could not be obtained with TEM. Regardless, EDX results illustrated the power of elemental mapping overlays with grayscale images. Areas of high contrast were shown to be silver against a background composed predominately of carbon and oxygen. EDX was also able to eliminate other areas of high contrast by determining they were caused by surface charging or contamination from the sample preparation room. Due to the geometry and beam sampling limitations discussed previously, quantitative elemental analysis was not attempted.

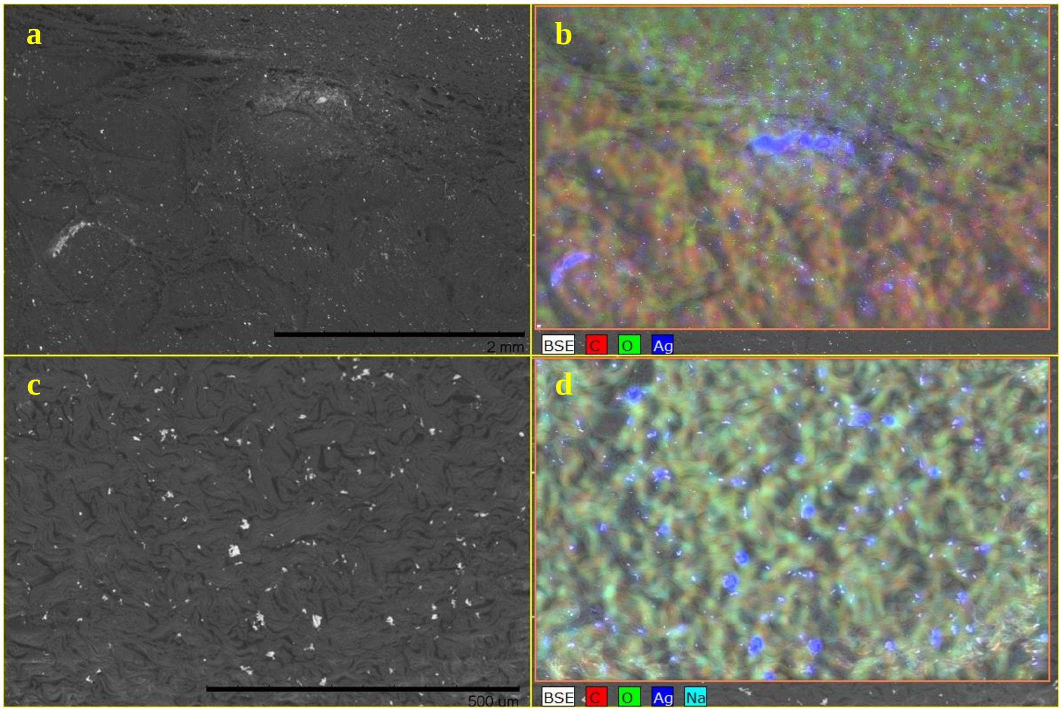

Fig. 16 SEM images and EDX maps from the surface of the sample in Cassette 5. Scale bars are 2 mm (a) and 500 µm (b)

3.2 Experimental Trial

Representative TEM images of Cassettes 2 and 11 containing the pig skin collected from sites adjacent to control and test article sites are shown in Fig. 17. The control article showed at low magnification (micrograph a Fig. 17) notable amounts of intracellular (asterisks) and extracellular (arrows) AgNP aggregates. A higher magnification (micrograph b Fig. 17) showed accumulations of AgNPs within a phagocytic cell (asterisks) and within a collagen matrix (arrows). The test article showed at low magnification (micrograph c Fig. 17) an admixture of inflammatory cells including macrophages (m), neutrophils (n), lymphocytes (l), and phagocytes (p); however, AgNPs were not noted. Higher magnification (micrograph d Fig. 17) showed an aggregate of AgNPs (asterisk) and scattered singular AgNPs throughout an acellular, serous substrate at the tissue-device interface. Many of the aggregates were noted within phagocytic cells, while smaller collections of AgNPs were typically noted in interstitial spaces or within the connective tissue deposited in response to the device's presence. AgNP aggregates were much less prominent in the test site. Some singular AgNPs were noted in interstitial spaces.

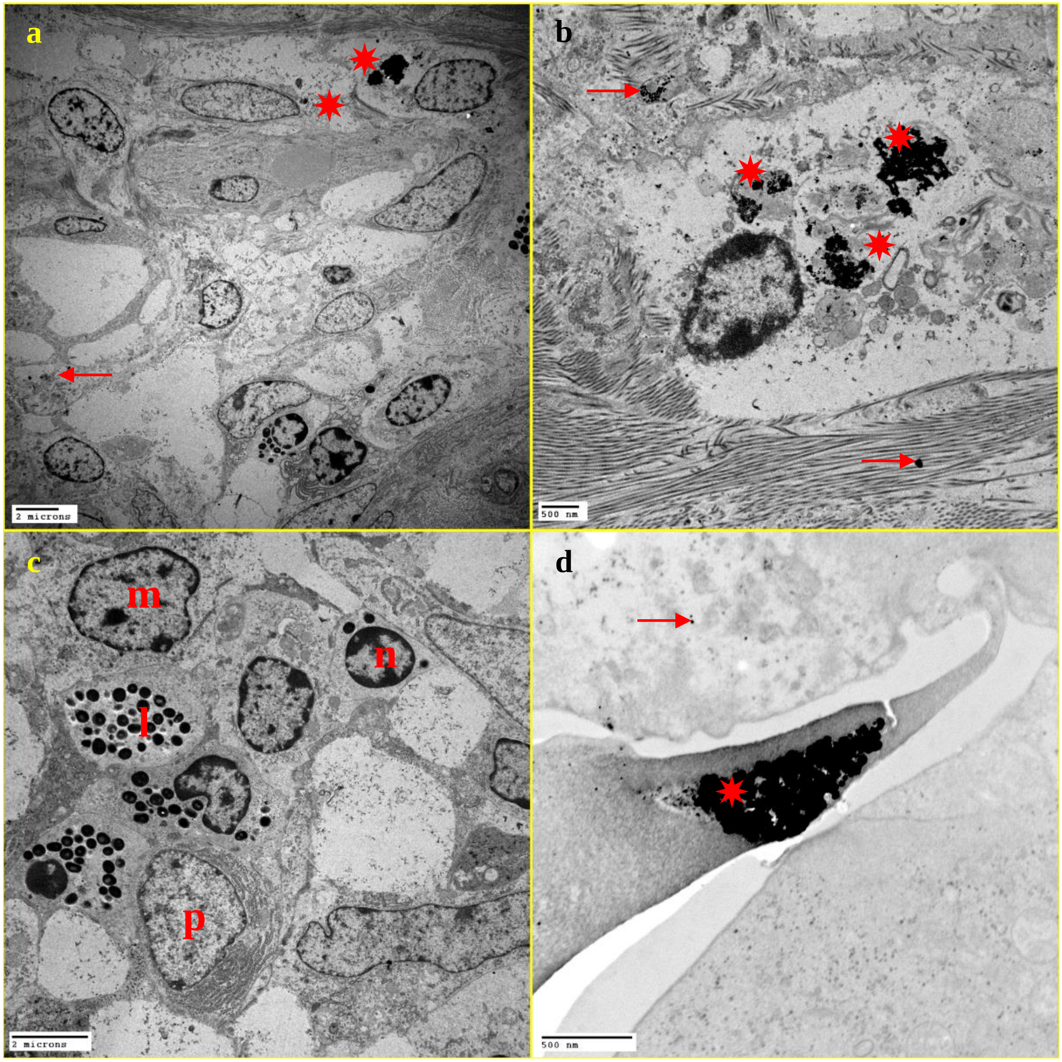

Fig. 17 Representative TEM findings for test and control samples in the experimental trial. Scale bars are 2 µm (a,c) and 500 nm (b,d)

Cassettes 3, 6, 9, 12, 15, and 18 were subjected to INAA; results from automated spectrum analysis using GENIE™ are shown in Table 5. The mass of silver in each standard was calculated using the 987 ppm silver concentration reported in their documentation. The amount of silver from the control sample in Cassette 12 was calculated using both 657 and 884 keV peaks with each standard and Eq. 2. Results of these calculations along with the SNR for each peak are shown in Table 6.

Table 5 Peak analysis results using GENIE™ for the standard and sections of tissue subjected to INAA during the experimental trial. Data for cassettes taken from tissue adjacent to the control article are highlighted

Sample Descriptor	Total Sample Mass [g]	Silver Mass [µg]	657 keV Peak Area [counts]	884 keV Peak Area [counts]
Standard	0.2520	248.7	684 ± 28.57	373 ± 21.38
Cassette 3	0.3034	N/A	N/A	N/A
Cassette 6	0.2210	N/A	N/A	N/A
Cassette 9	0.3102	N/A	N/A	N/A
Cassette 12	0.2799	N/A	56.7 ± 16.51	28.0 ± 14.52
Cassette 15	0.2304	N/A	N/A	N/A
Cassette 18	0.3438	N/A	N/A	N/A

Table 6 The amount of silver present in Cassette 12 from the experimental samples. SNR for each peak is also included

	Cassette 12	SNR
657 keV Peak	20.62 ± 6.07 µg	0.7
884 keV Peak	18.67 ± 9.74 µg	0.4

Silver was only detectable in the sample taken from the site most adjacent to the control sample, Cassette 12. Silver content was determined to be 18.67 µg within the 280 mg sample, or approximately 67 ppm, based on the 884 keV peak, but this determination had a 52% error. Using the 657 keV peak resulted in a silver amount of

20.62 μg within the 280 mg sample, or approximately 74 ppm, with a smaller error of 29%. The SNR for the 657 keV peak was also nearly double that of the 884 keV peak; however, SNRs were consistently lower than those observed during the feasibility trial. Background noise was greatly reduced by replacing the sodium phosphate buffered fixative solution in the samples with ethanol prior to irradiation and allowing the activated sodium longer to decay between the end of irradiation and start of gamma ray acquisition. Signal was reduced to a greater extent, however, due to the much lower content of silver in the experimental sample and the shorter irradiation time. These observations are supported by the comparison of gamma ray spectra shown in Fig. 18. The most prominent feature noted for Cassette 3 (spectrum b Fig. 18) is the Compton continuum caused by the strong presence of ^{24}Na. Contrarily, ^{24}Na is not as prominently present for Cassette 12 (spectrum a Fig. 18).

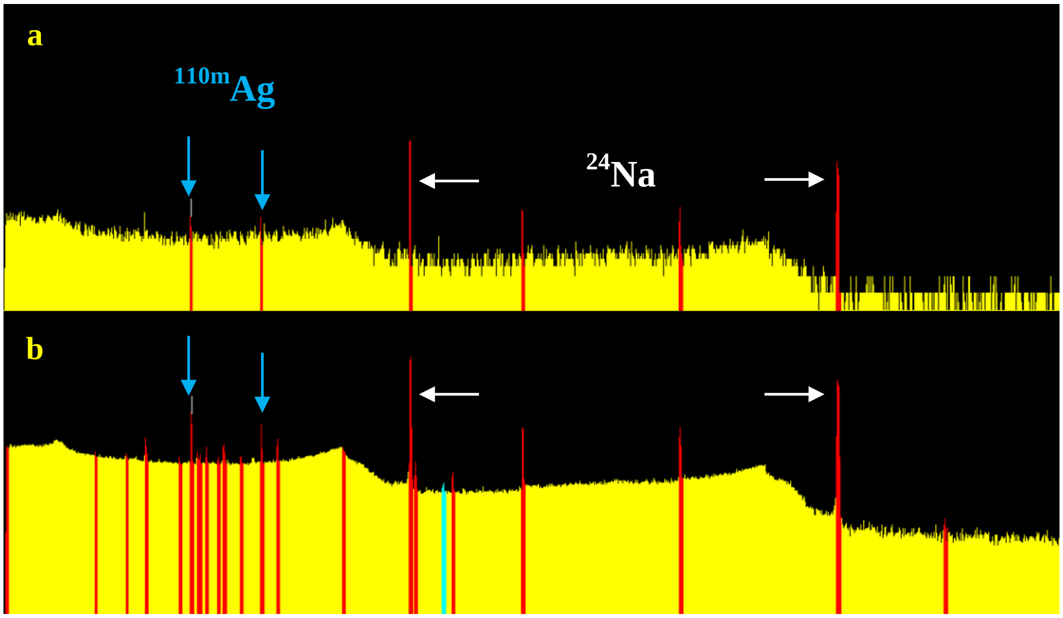

Fig. 18 Gamma ray spectra from Cassette 12 in the experimental trial (top) and Cassette 3 in the feasibility trial (bottom). Abscissae are energy and ordinates are net counts. The ^{110m}Ag and ^{24}Na peaks used in the analysis are noted by blue and white arrows, respectively

SEM with EDX showed little difference between the surfaces of samples taken from adjacent to the control and test articles. Representative images of this analysis are shown in Fig. 19. A single area of high contrast was found on the control sample from Cassette 10. The high contrast area consisted of an aggregation of granular particles embedded within the tissue (micrograph c red circle Fig. 19) that emitted a strong characteristic silver X-ray signal when analyzed with EDX (spectrum d Fig. 19). The area measured approximately 10 µm in greatest dimension, however, and was not representative of the entire area analyzed. EDX was able to eliminate other areas of high contrast by determining the cause was surface charging or contamination from the sample preparation room.

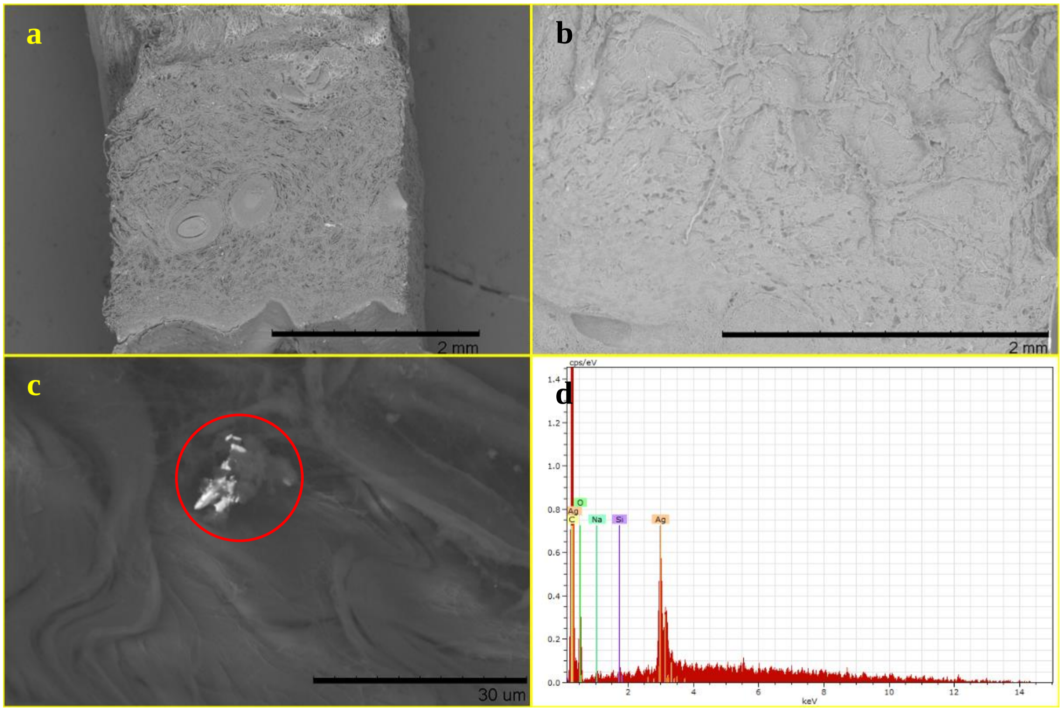

Fig. 19 Representative SEM images from the control (a) and test (b) articles. An area of the control article (c, red circle) was analyzed with EDX. Scale bars are 2 mm (a,b) and 30 μm

3.3 Simulation

Three fluence rate schemes were tested with the model. The areas predicted by the model for the 657 keV peak were compared to net peak areas measured for various activation and decay times used in the feasibility and experimental trials. Eq. 30 was used to calculate the degree of agreement between experimental and simulation results as shown in Table 7. The measured, simulated, and resonance-corrected fluence schemes predicted 657 keV peak areas with average errors of 15.0 ± 15.3%, 24.5 ± 27.8%, and 19.0 ± 6.9%, respectively. While the degree of difference between predicted and measured values had a lower average error using the measured fluence scheme, the resonance-corrected fluence scheme was chosen for the remainder of the simulations due to the much lower standard deviation of errors in the predictions. This scheme considered fluence rate as two-group with thermal and resonance components of 1.02×10^{13} and $1.97\text{E}\times10^{10}$ $\text{n}\cdot\text{cm}^{-2}\cdot\text{s}^{-1}$, respectively.

Table 7 Fluence rate schemes tested during model benchmarking and the calculated agreement metric values. The average and standard deviation of all the metrics for the resonance-corrected fluence rate scheme are highlighted

	Measured		**Simulated**		**Resonance-Corrected**	
	Thermal	**Epithermal**	**Thermal**	**Epithermal**	**Thermal**	**Resonance**
[$\text{n}\cdot\text{cm}^{-2}\cdot\text{s}^{-1}$]	7.50E+12	2.40E+11	1.02E+13	2.37E+11	1.02E+13	1.97E+10
Sample Descriptor	**657 keV Peak**	**884 keV Peak**	**657 keV Peak**	**884 keV Peak**	**657 keV Peak**	**884 keV Peak**
Standard A	0.066	0.178	0.148	0.011	0.150	0.252
Standard B	0.092	0.144	0.116	0.052	0.173	0.221
Skin	0.407	0.384	0.729	0.701	0.280	0.260
Standard	0.164	0.091	0.027	0.117	0.239	0.172
Cassette 12	0.020	0.177	0.204	0.446	0.108	0.071
Average	***0.150***	***0.195***	***0.245***	***0.265***	***0.190***	***0.195***
Std. Dev.	***0.153***	***0.112***	***0.278***	***0.298***	***0.069***	***0.077***

Once the appropriate fluence rates were determined, the complex and simple models were compared by using them to predict ^{110m}Ag inventories at 7 d following the beginning of irradiation and applying Eq. 31. Results of this analysis are shown in Fig. 20. The degree of difference between the models increased linearly with a perfect correlation as the fraction of analysis time spent irradiating the samples increased. Thus, the simple model was believed to become less accurate if used to simulate samples with longer irradiation times and shorter decay times. According to the trend line equation in

Fig. 20, the maximum amount of theoretical error in predicted ^{110m}Ag inventory that may have been introduced by assuming the simple model was approximately 0.05%. This was thought to be negligible in comparison to the error of 20% associated with the fluence rate values chosen for the model. Therefore, the simple model was thought to predict ^{110m}Ag activity just as well as the complex model for the purposes of this research.

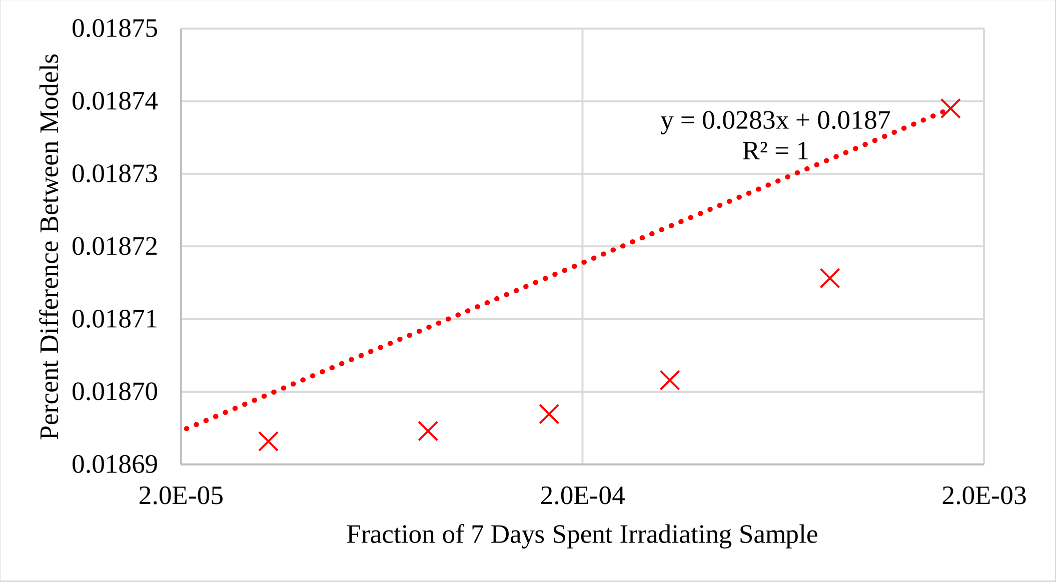

Fig. 20 Comparison of how the complex and simple models differ in predicting ^{110m}Ag inventory for various activation schemes. The dotted line shows the linear relationship described by the trend line equation. Data points were calculated using Eq. 31 and are shown as red “X” markers

The simple model was used to calculate ^{110m}Ag and ^{24}Na inventories for the approximate activation schemes used in the feasibility and experimental trials. The results were compared to schemes thought to be advantageous for future work. Fifty micrograms of silver and 100 and 200 µg of sodium were input to the model. T_{EOI} was the irradiation time, and T_{Total} was the total amount of time that the sample was irradiated, allowed to decay, and counted for 600 s. Results are shown in Table 8. A graphical summary of results is shown in Fig. 21.

Table 8 Simulated peak areas for ^{110m}Ag and ^{24}Na for various irradiation times. Parameters used for the feasibility and experimental trials are highlighted in gray

		Simulated Peak Area [counts]			
T_{EOI} [s]	**T_{Total}**	**657 keV**	**884 keV**	**1368 keV**	**2753 keV**
60	18 hours	160	95	35455	19515
40	6 days	105	62	71	39
60	6 days	157	93	106	59
60	7 days	157	93	35	19
120	7 days	313	186	70	39

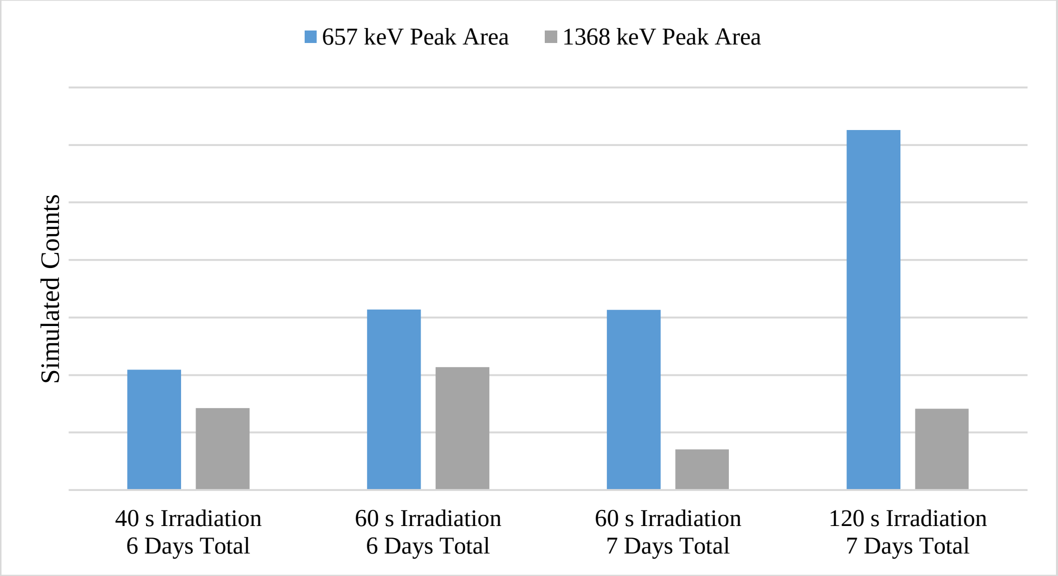

Fig. 21 Simulated peak areas for the 657 keV ^{110m}Ag and 1368 keV ^{24}Na peaks for various irradiation schemes. The feasibility trial simulation is not included

Assuming the ability to quantify silver depended mainly on SNR for the 657 keV peak, and the noise under the peak was primarily caused by the Compton continuum from the 1368 keV ^{24}Na peak, Table 8 and Fig. 21 show that decay time was the primary factor governing the ability to quantify silver in these types of biological matrices. In the experimental trial T_{EOI} was 40 s and the samples were allowed to decay for approximately 6 d. The simulation showed that increasing irradiation time to 60 s made the samples more radioactive, but the difference between the intensities of the 657 and 1368 keV peaks did not change by much. Allowing the samples to decay for 7 d after 60 s of irradiation, however, greatly decreased ^{24}Na activity. Thus, increasing decay time from 6 to 7 d would greatly increase the ability to quantify silver in these types of samples. Doubling irradiation time to 120 s prior to allowing approximately 7 d of decay increased the areas under each peak as expected, but also increased the ratio between the intensity of the two. Fig. 22 was generated using output from the simulation and shows the relationship between the 657 and 1368 keV gamma rays detected from ^{110m}Ag and ^{24}Na at various times following 120 s of irradiation of 50 µg of silver and 100 and 200 µg of sodium. These data could be used to predict ratios of silver and sodium peak areas for various irradiation timing schemes for improved design of future experiments.

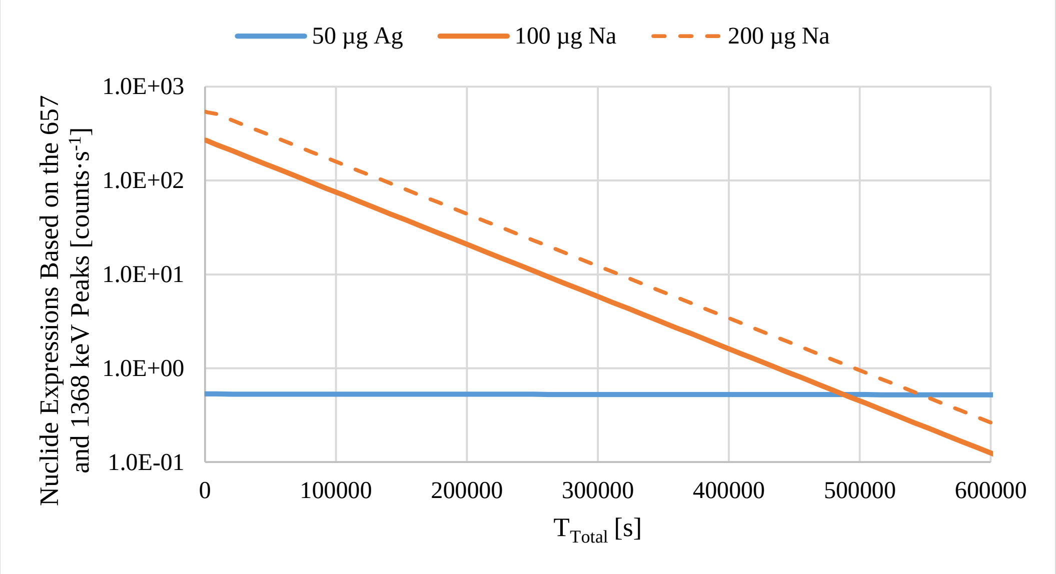

Fig. 22 Comparison of detectable gamma ray ratios from ^{110m}Ag and ^{24}Na following irradiation of 50 µg of silver with 100 or 200 µg of sodium

4. CONCLUSIONS

TEM analysis of AgNP-containing skin samples yielded qualitative results of host reaction to AgNPs. In the experimental trial, inflammatory cells exhibited an expected reaction to the presence of a device at 43 d post-implant. Phagocytic cells appeared to scavenge larger aggregates of AgNPs in control samples where silver content was known to be higher. Test samples contained less observable AgNPs and inflammatory cells displayed little reaction to the presence of smaller AgNP aggregates.

Quantitative results from INAA in the experimental trial reinforced observations made with TEM. Silver was not detected within samples taken adjacent to the device with the coating that was hypothesized to not elute silver. A silver concentration of 74 ppm ± 29% was measured in a sample taken adjacent to the control article that was known to elute silver. The relatively high error associated with this measurement was attributed to the noise generated by ^{24}Na content of the sample during gamma ray spectroscopy.

The Simulink® model built to compute silver activation progeny inventories was used to relate the poor SNR encountered during feasibility and experimental trials to the 657 keV ^{110m}Ag and 1368 keV ^{24}Na peak areas. The model showed that decay time following irradiation was the major factor predicting the ability to measure silver in biological matrices via INAA.

In future work involving investigation of silver in these types of samples, it is recommended to increase activation time from 60 to 120 s to significantly increase the intensity of the 657 keV ^{110m}Ag peak relative to background. This would allow for a more specific measurement of the amount of silver present in samples with a lower limit of detectability. It is also recommended to increase decay time to 7 d to allow ^{24}Na activity to almost completely deplete prior to measurement. Samples should also be dehydrated in multiple washes of ethanol prior to irradiation to reduce the amount of sodium in samples from fixative buffers.

For true correlation between INAA and TEM, irradiated samples could be processed for TEM following gamma ray spectroscopy. Dehydrating samples in ethanol prior to irradiation would benefit this process since ethanol dehydration is required for TEM sample processing. Research should be performed to assess the safety of this technique, since this would require INAA laboratories to release radioactive material to TEM laboratories for handling and sample preparation. Total activity of biological samples containing silver should be measured over time after irradiation to assess whether handling these types of samples poses any danger to technicians. Increasing SNR with longer irradiation and decay times may decrease the amount of bulk sample needed to measure silver concentrations, also reducing total radioactivity of samples following irradiation.

REFERENCES

1. Eiff C, Jansen B, Kohnen W and Becker K (2005) Infections associated with medical devices: pathogenesis, management, and prophylaxis. Drugs 65:179-214.

2. Habash M and Reid G (1999) Microbial biofilms: their development and significance for medical device-related infections. Journal of Clinical Phamacology 39:887-898.

3. Zierer A, Spencer M, Voeller RK, Guthrie TJ, Ewald GA, et al. (2007) Late-onset driveline infections: the Achilles' heel of prolonged left ventrivular assist device support. Annals of Thoracic Surgery 84:515-521.

4. Holman WL, Kirklin JK, Naftel DC, Kormos RL, Desvign-Nickens P, et al. (2010) Infection after implantation of pulsatile mechanical circulatory support devices. Journal of Thoracic and Cardiovascular Surgery 139:1632-1636.

5. Choi L, Choudhri AF, Pillarisetty VG, Sampath LA, Caraos L, et al. (1999) Development of an infection-resistant LVAD driveline: a novel approach to the prevention of device-related infections. Journal of Heart and Lung Transplantation 18:1103-1110.

6. Holman WL, Rayburn BK, McGiffin DC, Foley BA, Benza RL, et al. (2003) Infection in ventricular assist devices: prevention and treatment. Annals of Thoracic Surgery 75:S48-S57.

7. Kirklin JK, Naftel DC, Kormos RL, Stevenson LW, Pagani FD, et al. (2010) Second INTERMACS annual report: more than 1,000 primary left ventricular assist device implants. Journal of Heart and Lung Transplantation 29:1-10.

8. Maniar S, Kondareddy S and Topkara VK (2011) Left ventricular assist device-related infections: past, present and future. Expert Reviews of Medical Devices 8:627-634.

9. Jansen B, Rinck M, Wolbring P, Strohmeier A and Jahns T (1994) In vitro evaluation of the antimicrobial efficacy and biocompatability of a silver-coated central venous catheter. Journal of Biomaterials Applications 9:55-70.

10. Reidy B, Haase A, Luch A, Dawson KA and Lynch I (2013) Mechanisms of silver nanoparticle release, transformation and toxicity: a critical review of current knowledge and recommendations for future studies and applications. Materials 6:2295-2350.

11. Marambio-Jones C and Hoek EMV (2010) A review of the antibacterial effects of silver nanomaterials and potential implications for human health and the environment. Journal of Nanoparticle Research 12:1531-1551.

12. Choi O, Deng KK, Kim N-J, Ross L, Surampalli RY, et al. (2008) The inhibitory effects of silver nanoparticles, silver ions, and silver chloride colloids on microbial growth. Water Research 42:3066-3074.

13. United States Food and Drug Administration (2007) Draft guidance for industry and FDA staff: Premarket notification [510(k)] submissions for medical devices that include antimicrobial agents. Center for Devices and Radiological Health. Rockville, MD.

14. Hillyer JF and Albrecht RM (1999) Correlative instrumental neutron activation analysis, light microscopy, transmission electron microscopy, and X-ray microanalysis for qualitative and quantitative detection of colloidal gold spheres in biological specimens. Microscopy and Microanalysis 4:487-490.

15. Ayache J, Beaunier L, Boumendil J, Ehret G and Laub D (2010) Sample preparation handbook for transmission electron microscopy, 2 edn. Springer, New York, NY.

16. Facility AMaMR (2012) MyScope training for advanced research. http://www.ammrf.org.au/myscope. Accessed 27 Feb 2014.

17. Lorimer GW (1987) Quantitative X-ray microanalysis of thin specimens in the transmission electron microscope: a review. Mineralogical Magazine 51:49-60.

18. Newbury DE and Ritchie NWM (2012) Is scanning elecron microscopy/energy dispersive X-ray spectrometry (SEM/EDS) quantitative? Scanning 00:1-28.

19. Greenberg RR, Bode P and Fernandes EAD (2011) Neutron activation analysis: a primary method of measurement. Spectrochimica Acta Part B 66:193-241.

20. Win DT (2004) Neutron activation analysis (NAA). Australian Journal of Technology 8:8-14.

21. Adams F, Hoste J and Speecke A (1963) Determination of silver in lead by neutron activation analysis. Talanta 10:1243-1249.

22. Albini A, Cesana A and Terrani M (1976) Determination of silver traces in air by neutron activation analysis. Journal of Radioanalytical Chemistry 34:185-190.

23. Sujari ANA and Bowen HJM (1987) Determination of silver in foods by neutron activation analysis. Journal of the Science of Food and Agriculture 38:367-372.

24. Randa Z and Kucera J (2003) Trace elements in higher fungi (mushrooms) determined by activation analysis. Journal of Radioanalytical and Nuclear Chemistry 259:99-107.

25. Gordus AA (1967) Quantitative non-destructive neutron activation analysis of silver in coins. Archaeometry 10:78-86.

26. Swain KK, Ajith N, Acharya R, Verma R and Reddy AVR (2012) Large sample neutron activation analysis of dross for gold and silver. Journal of Radioanalytical and Nuclear Chemistry 294:319-322.

27. Pun TH and Landsberger S (2012) Determination of silver using cyclic epithermal neutron activation analysis. Journal of Radioanalytical and Nuclear Chemistry 291:509-513.

28. Pantelica A, Ene A and Georgescu II (2012) Instrumental neutron activation analysis of some fish species from Danube River in Romania. Microchemical Journal 103:142-147.

29. Fukushima M and Chatt A (2013) Rapid determination of silver in cultivated Japanese and South Korean oysters and Japanese rock oysters using the 24.6-s neutron activation product 110Ag and estimation of its average daily intake. Journal of Radioanalytical and Nuclear Chemistry 296:563-571.

30. Chadwick MB, Herman M, Oblozinský P, Dunn ME, Danon Y, et al. (2011) ENDF/B-VII.1 nuclear data for science and technology: cross sections, covariances, fission product yields and decay data. Nuclear Data Sheets 112:2887-2996. Accessed via Janis 3.2.

31. Center BNLNND (2014) Chart of Nuclides. http://www.nndc.bnl.gov/chart/. Accessed 30 April 2014.

32. Dykstra MJ and Reuss LE (2003) Biological electron microscopy: theory, techniques, and troubleshooting, 2 edn. Springer, New York, NY.

33. Koning AJ, Rochman D, Marck SC, Kopecky J, Sublet JC, et al. (2013) http://www.talys.eu/tendl-2013. TENDL-2013: TALYS-based evaluated nuclear data library. Nuclear Research and Consultancy Group. Petten, The Netherlands. Accessed via Janis 3.2.

34. Nakamura S, Wada H, Shcherbakov O, Furutaka K, Harada H, et al. (2003) Measurement of the thermal neutron capture cross section and the resonance integral of the 109Ag(n,γ)110mAg reaction. Journal of Nuclear Science and Technology 40:119-124.

35. Parham NA (2010) Development of real-time fuel management capability at the Texas A&M nuclear science center. Department of Nuclear Engineering, Texas A&M University, College Station, TX.

36. Verheijke ML (2000) On the relations between the effective resonance energy and the infinite dilution resonance integral for (n,γ) reactions. Journal of Radioanalytical and Nuclear Chemistry 246:161-163.

APPENDIX A

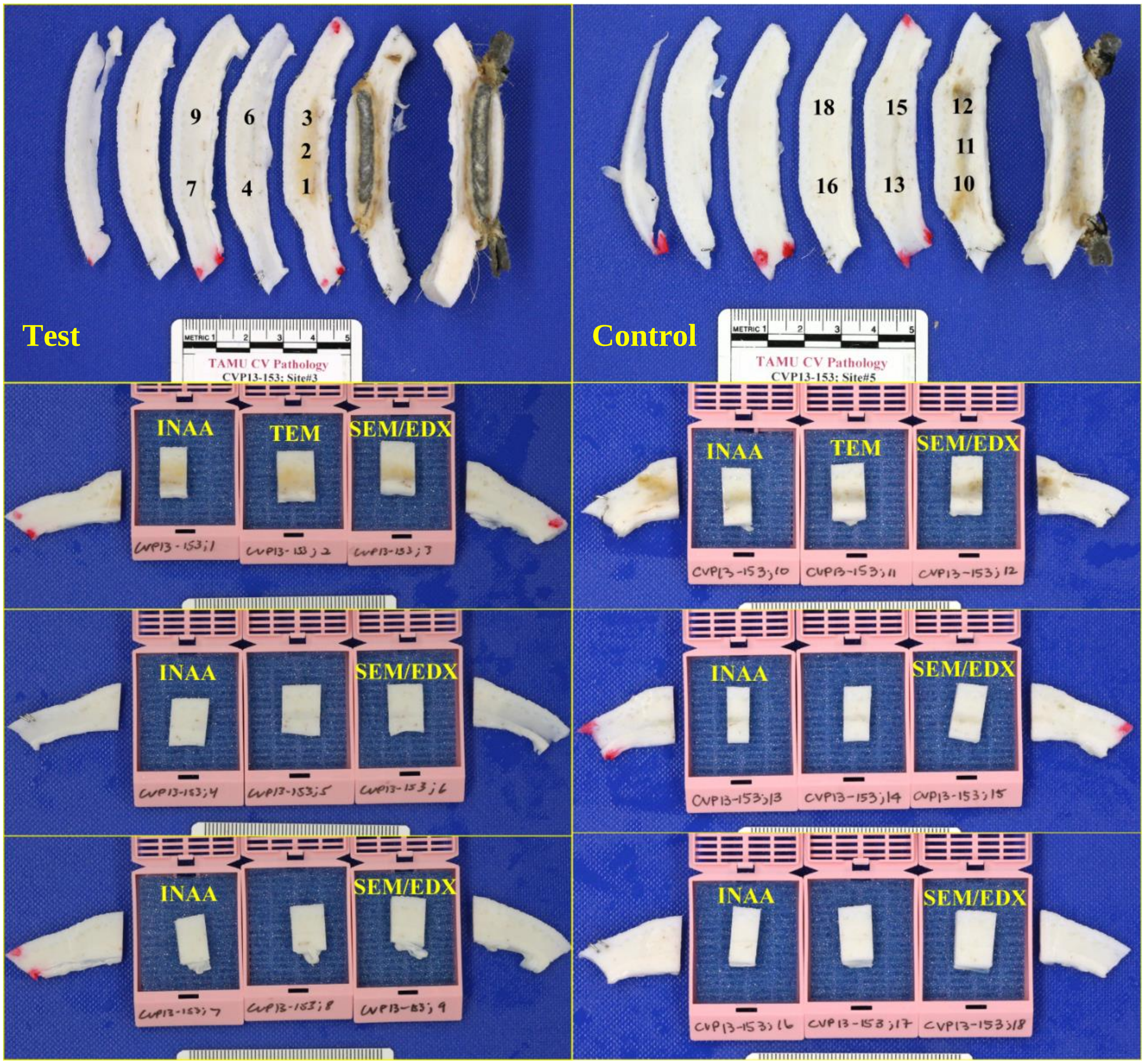
9
6
3
2
1
7
4
Test
METRIC 1 2 3 4 5
TAMU CV Pathology
CVP13-153; Site#3
INAA
TEM
SEM/EDX
CVP13-153;1
CVP13-153;2
CVP13-153;3
INAA
SEM/EDX
CVP13-153;4
CVP13-153;5
CVP13-153;6
INAA
SEM/EDX
CVP13-153;7
CVP13-153;8
CVP13-153;9
18
15
12
11
16
13
10
Control
METRIC 1 2 3 4 5
TAMU CV Pathology
CVP13-153; Site#5
INAA
TEM
SEM/EDX
CVP13-153;10
CVP13-153;11
CVP13-153;12
INAA
SEM/EDX
CVP13-153;13
CVP13-153;14
CVP13-153;15
INAA
SEM/EDX
CVP13-153;16
CVP13-153;17
CVP13-153;18

APPENDIX B

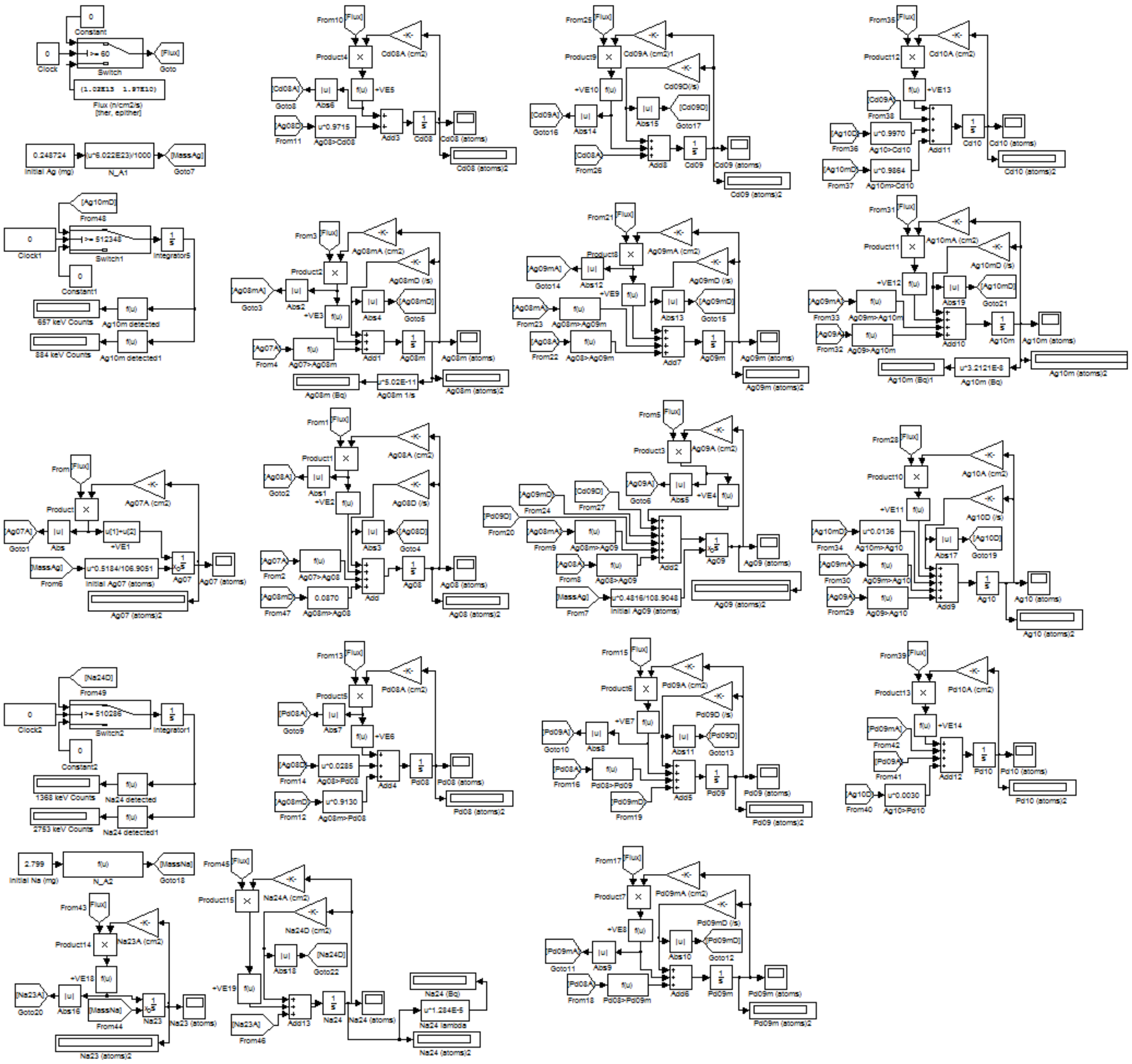

APPENDIX C

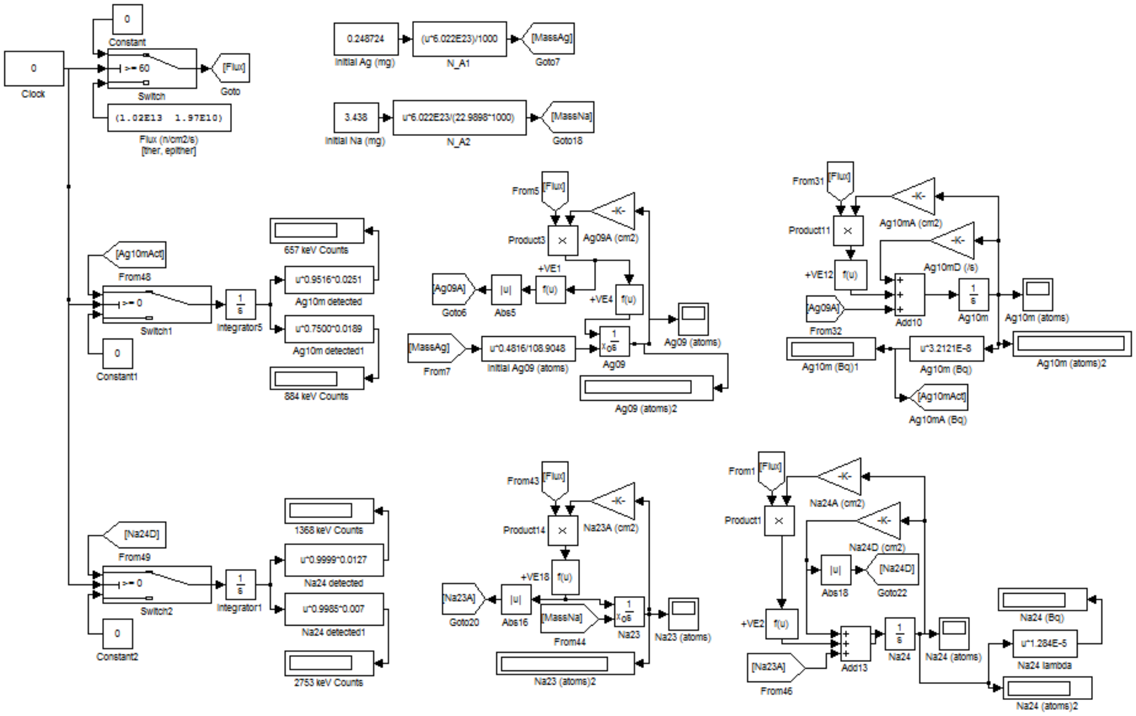

0
Constant
0
Clock
>= 60
Switch
[Flux]
Goto
(1.02E13 1.97E10)
Flux (n/cm2/s)
[ther, epither]
0.248724
Initial Ag (mg)
(u*6.022E23)/1000
N_A1
[MassAg]
Goto7
3.438
Initial Na (mg)
u*6.022E23/(22.9898*1000)
N_A2
[MassNa]
Goto18
[Ag10mAct]
From48
>= 0
Switch1
0
Constant1
1/s
Integrator5
657 keV Counts
u*0.9516*0.0251
Ag10m detected
u*0.7500*0.0189
Ag10m detected1
884 keV Counts
From5
[Flux]
-K-
Ag09A (cm2)
Product3
×
+VE1
f(u)
[Ag09A]
Goto6
|u|
Abs5
+VE4
f(u)
[MassAg]
From7
u*0.4816/108.9048
Initial Ag09 (atoms)
1/s
Ag09
Ag09 (atoms)
Ag09 (atoms)2
From31
[Flux]
-K-
Ag10mA (cm2)
Product11
×
-K-
Ag10mD (/s)
+VE12
f(u)
[Ag09A]
From32
Add10
1/s
Ag10m
Ag10m (atoms)
Ag10m (Bq)1
u*3.2121E-8
Ag10m (Bq)
Ag10m (atoms)2
[Ag10mAct]
Ag10mA (Bq)
[Na24D]
From49
>= 0
Switch2
0
Constant2
1/s
Integrator1
1368 keV Counts
u*0.9999*0.0127
Na24 detected
u*0.9985*0.007
Na24 detected1
2753 keV Counts
From43
[Flux]
-K-
Na23A (cm2)
Product14
×
+VE18
f(u)
[Na23A]
Goto20
|u|
Abs16
[MassNa]
From44
1/s
Na23
Na23 (atoms)
Na23 (atoms)2
From1
[Flux]
-K-
Na24A (cm2)
Product1
×
-K-
Na24D (cm2)
|u|
Abs18
[Na24D]
Goto22
+VE2
f(u)
[Na23A]
From46
Add13
1/s
Na24
Na24 (atoms)
Na24 (Bq)
u*1.284E-5
Na24 lambda
Na24 (atoms)2